



A 3D common-refinement method for non-matching meshes in partitioned variational fluid–structure analysis

Yulong Li, Yun Zhi Law, Vaibhav Joshi, Rajeev K. Jaiman *

Department of Mechanical Engineering, National University of Singapore, 119077, Singapore

ARTICLE INFO

Article history:

Received 17 June 2017

Received in revised form 8 May 2018

Accepted 12 May 2018

Available online 16 May 2018

Keywords:

Fluid–structure interaction

3D common-refinement

Non-matching meshes

Partitioned staggered

Nonlinear iterative force correction

Petrov–Galerkin finite element

ABSTRACT

We present a three-dimensional (3D) common-refinement method for non-matching unstructured meshes between non-overlapping subdomains of incompressible turbulent fluid flow and nonlinear hyperelastic structure. The fluid flow is discretized using a stabilized Petrov–Galerkin method, and the large deformation structural formulation relies on a continuous Galerkin finite element method. An arbitrary Lagrangian–Eulerian formulation with a nonlinear iterative force correction (NIFC) coupling is achieved in a staggered partitioned manner by means of fully decoupled implicit procedures for the fluid and solid discretizations. To begin, we first investigate the accuracy of common-refinement method (CRM) to satisfy the traction equilibrium condition along the fluid–elastic interface with non-matching meshes. We systematically assess the accuracy of CRM against the matching grid solution by varying grid mismatch between the fluid and solid meshes over a tubular elastic body. We demonstrate the second-order accuracy of CRM through uniform refinements of fluid and solid meshes along the interface. We then extend the error analysis to transient data transfer across non-matching meshes between the fluid and solid solvers. We show that the common-refinement discretization across non-matching fluid–structure grids yields accurate transfer of the physical quantities across the fluid–solid interface. We next solve a 3D fluid–structure interaction (FSI) problem of a cantilevered hyperelastic plate behind a circular bluff body and verify the accuracy of coupled solutions with respect to the available solution in the literature. By varying the solid interface resolution, we generate various non-matching grid ratios and quantify the accuracy of CRM for the nonlinear structure interacting with a laminar flow. We illustrate that the CRM with the partitioned NIFC treatment is stable for low solid-to-fluid density ratio and non-matching meshes for the 3D FSI problem. Finally, we demonstrate the 3D parallel implementation of the common-refinement with the NIFC method for a realistic engineering problem of drilling riser undergoing complex vortex-induced vibration with strong added mass effects and turbulent wake flow.

© 2018 Elsevier Inc. All rights reserved.

1. Introduction

Many scientific and engineering simulations that involve interaction of multiple physical fields often require an accurate method to transfer the physical data across non-matching discrete meshes. These problems include electromagnetics [1,2],

* Corresponding author.

E-mail address: mperk@nus.edu.sg (R.K. Jaiman).

contact dynamics [3–5], conjugate heat transfer [6], and fluid–structure interaction (FSI) [7]. In particular, FSI applications generally rely on different mesh requirements for fluid and solid subdomains to capture the interaction physics accurately, which involves multiple scales and complex multi-modal coupled dynamics. Such requirements of non-matching meshes are common in FSI applications spanning from aircraft wings, deep-water drilling riser, mooring lines, tendons and subsea pipelines [8–10] to blood flow in arteries and various biomechanical problems. A data transfer with locally inaccurate interpolation and projection may lead to poor estimation of fluid–elastic response and instability prediction, especially when the response frequency is close to the natural frequency of the structure. Henceforth, high-fidelity coupled fluid–structure simulations require an accurate treatment of interface boundary conditions across non-matching surface meshes.

For body-fitted Eulerian–Lagrangian coupling, two main approaches exist for the numerical modeling of FSI problems, namely monolithic [11–15] and partitioned [16–20]. In the monolithic approach, the flow and structure equations are solved together in a fully coupled manner by assembling the coupled equations into a single block [11,13,12]. While the monolithic formulations offer good numerical stability for problems involving very strong added mass effects, the schemes lack the advantage of flexibility and modularity of using existing stable fluid or structural solvers [13,14,21]. On the other hand, the partitioned schemes solve the fluid and structure equations in a sequential manner over two decomposed subdomains [22,19], facilitating the coupling of the existing fluid and structural codes with suitable choices of spatial and temporal discretizations. However, partitioned schemes may suffer from numerical instability and convergence issues during strong fluid–structure coupling especially when structure-to-fluid density ratio is low (e.g., heavy liquid interacting with a light buoyant structure). Many approaches have been developed to address this issue, which includes the nonlinear iterative force correction (NIFC) scheme [23], the continuous projection method [24,25], the fictitious mass and damping [26], the block-LU factorization [27,28] and the kinematically coupled scheme [29]. Typically, the partitioned schemes can be classified as either strongly-coupled [30,31,23] or loosely-coupled [22,18]. A strongly-coupled scheme attempts to satisfy the velocity continuity and the traction equilibrium across the fluid–structure interface via nonlinear iterations, unlike a loosely-coupled scheme which has a single exchange of interface conditions between the fluid and the structure within a time step. In both approaches, the surface boundary data must be exchanged or transferred through the interface meshes between the fluid and structure subdomains.

In a typical partitioned-based FSI simulation, surface meshes at the fluid–structure interface are generally non-matching [7,17,32]. This means that their connectivity arrangements are different, and their geometric coordinates may not be coincident due to discretization requirements. Such non-matching meshes and associated data transfer problems also exist in other situations [33], such as adaptive meshing and multi-grid considerations. In the present contribution, we focus on the 3D parallel implementation of the common-refinement method based on the weighted residual or ℓ_2 minimization process [34] to handle the data transfer across interfaces in our strongly-coupled FSI framework [23]. There are two main questions one needs to answer when dealing with the spatial coupling methods across non-matching meshes [7,35]: (a) How to interpolate and project tractions accurately along the fluid–solid interface with non-matching meshes? (b) How to integrate the traction vector defined on the fluid mesh over the interface elements of solid mesh with their respective shape functions? In [7,35], a detailed survey of point-to-element and common-refinement based method was provided for one-dimensional (1D) and two-dimensional (2D) problems with both flat and curved boundaries. It was demonstrated that the point-to-element methods can lead to significant errors and sensitivity to grid-mismatch due to a violation of the regularity of quadrature rule. These errors can be non-convergent during simultaneous grid refinement of fluid and solid input meshes and can impact the local accuracy along the fluid–solid interface.

A common-refinement overlay mesh is essentially a surface mesh composed of elements that subdivide the elements of both fluid and solid input meshes simultaneously [36,37], or simply the intersections of the elements of the input meshes. The common-refinement discretization enables accurate integration of functions that depend on the shape functions of the two disparate mesh realizations [7,35,38]. By constructing such topological intersection of the source and target meshes, consistency of the numerical integration can be obtained by performing the quadrature integration over the common-refinement overlay surface. The common-refinement overlay mesh is constructed such that both the source functions and the target functions are continuous in each of its elements, thus yielding the accurate integration process. For these reasons, the common-refinement method is important for the computations of fluid–structure interaction. This method is deemed desirable but can be somewhat complicated to implement in three dimensions as compared to other simple nearest neighbor or point-to-element projection methods. Therefore, it has been avoided by application scientists and engineers in their coupled partitioned multiphysics and multiscale analysis. Indeed it is challenging to compute a common-refinement surface since the geometrical realizations of the meshes are defined by distinct surfaces with arbitrary mesh intersections. Detailed computational geometry issues related to the construction of common-refinement of two three-dimensional discrete surfaces with curvature and sharp features are provided in [37,39].

The objectives of this paper are two folds. The first is to quantify the error introduced by the 3D common-refinement and compare the precision against the matching reference counterpart. The scope of the present work is to remove the necessity of matching meshes and to redesign a more general projection method for non-matching fluid and solid nodes along curved three-dimensional surfaces. Earlier investigations in [35,7] were performed in one- and two-dimensional configurations and the fluid flow was considered to be compressible. As shown in [40,41] for a model elastic plate, the added mass of a compressible flow system has a strong dependency on the length of time interval, whereas the added mass of an incompressible system asymptotically approaches a constant value as the length of the time interval goes to zero. This fundamental difference in the behavior of compressible and incompressible flows has an implication on the design of par-

tioned staggered algorithms [23,42,43] and therefore it is worth investigating the stability of common-refinement method for an incompressible flow interacting with an elastic structure. Furthermore, in the earlier works [35,7], the common-refinement method was implemented for the two-dimensional finite-volume and finite-element discretizations for the fluid flow and the solid deformation, respectively. In the present study, we employ the 3D common-refinement interface between two consistent three-dimensional Galerkin-based variational formulations for fluid and solid subdomains. We systematically assess the accuracy and convergence of the 3D common-refinement for a circular cylinder tube problem in both static and transient situations.

The second objective of this work is to develop a novel hybrid method based on the common-refinement (CR) discretization and the nonlinear iterative force correction (NIFC) formulation [23] for large-scale FSI problems involving unsteady wake flow and strong added-mass effects. The proposed hybrid CR-NIFC method enables a general computational FSI framework, which integrates the ALE-based implicit filtered Navier–Stokes solver and the implicit nonlinear hyperelastic structural solver via partitioned staggered strategy [23,44]. While the nonlinear structure model is discretized using a continuous Galerkin finite element discretization, a fluid solver using Petrov–Galerkin finite element spatial discretization and semi-discrete time stepping has been considered for the filtered Navier–Stokes equations to describe an incompressible turbulent flow. The temporal discretizations of both the fluid and the structural equations are embedded in the generalized- α framework by employing the classical Newmark approximations in time [23]. Owing to the domain decomposition strategy in the partitioned iterative procedure, we independently construct the three-dimensional meshes for the fluid and the solid subdomains. The forces from the fluid are applied to the structural boundary as the surface tractions, and the structure displacements give a deformation of the fluid subdomain. During the nonlinear sequence transformation, approximate interface force corrections are dynamically formed through sub-iterations to satisfy the force equilibrium while maintaining the velocity continuity condition along the fluid–solid interface. This iterative sequence coupling relies on the generalized Aitken’s iterated Δ^2 process and the dynamic sequence parameter, which provides the desired fluid–structure stability at low structure-to-fluid mass ratio [23]. In a nutshell, the vital contributions of this work are as follows:

- Development of 3D parallel common-refinement method for incompressible turbulent flow interacting with a hyperelastic structure using the stabilized Petrov–Galerkin finite element framework and a generalized partitioned staggered coupling;
- Systematic analysis of the interface errors and their impact on the stability and robustness of our second-order spatial and temporal framework for FSI simulations;
- Stable integration of our 3D common-refinement scheme with the NIFC procedure for low structure-to-fluid mass ratio problems;
- Illustration of our novel hybrid CR-NIFC for a long flexible marine riser interacting with a turbulent wake flow.

The organization of this manuscript is as follows. Section 2 summarizes the flow and the structural governing equations with interface coupling conditions. Section 3 gives the spatial discretization of the governing equations and the interface coupling conditions. Discretization details of the common-refinement method and the NIFC-based coupling procedure are described in Section 4. A systematic study on the spatial accuracy of the common-refinement method is presented in Section 5, which is followed by the demonstration of the accuracy of the common-refinement method for the FSI benchmark of cylinder-bar problem in Section 6. Section 7 gives a realistic engineering application of long flexible riser using the coupled framework based on the common-refinement and the NIFC schemes. Finally, the work is concluded with some key findings in Section 8.

2. Governing fluid–structure equations

Before the presentation of the 3D common-refinement method, we provide for completeness a brief review of the fluid–structure system. The governing equations for the fluid are applied in an arbitrary Lagrangian Eulerian form while the dynamical structural equation is formulated in a Lagrangian way, and the interface conditions are enforced between the two physical fields.

2.1. Incompressible Navier–Stokes with ALE formulation

To simulate the interaction of incompressible fluid flow with a flexible structure, the body-fitted moving boundary based approach is considered in this study. Let $\Omega^f(t) \subset \mathbb{R}^d$ be a fluid subdomain at time t , where d is the space dimension. The motion of an incompressible viscous fluid in $\Omega^f(t)$ is governed by the Navier–Stokes equations given by

$$\rho^f \frac{\partial \bar{\mathbf{u}}^f}{\partial t} \Big|_{\bar{\mathbf{x}}} + \rho^f (\bar{\mathbf{u}}^f - \mathbf{w}^f) \cdot \nabla \bar{\mathbf{u}}^f = \nabla \cdot \bar{\boldsymbol{\sigma}}^f + \nabla \cdot \boldsymbol{\sigma}^{\text{sgs}} + \mathbf{b}^f, \quad \text{on } \Omega^f(t), \quad (1)$$

$$\nabla \cdot \bar{\mathbf{u}}^f = 0, \quad \text{on } \Omega^f(t), \quad (2)$$

where $\bar{\mathbf{u}}^f = \bar{\mathbf{u}}^f(\mathbf{x}^f, t)$ and $\mathbf{w}^f = \mathbf{w}^f(\mathbf{x}^f, t)$ represent the fluid and mesh velocities respectively, defined for each spatial fluid point $\mathbf{x}^f \in \Omega^f(t)$, ρ^f is the density of the fluid and \mathbf{b}^f is the body force applied on the fluid and $\boldsymbol{\sigma}^{\text{sgs}}$ represents the extra

stress term due to the subgrid filtering procedure for large eddy simulation. Here, $\bar{\sigma}^f$ is the Cauchy stress tensor for a Newtonian fluid, written as $\bar{\sigma}^f = -\bar{p}^f \mathbf{I} + \mu^f (\nabla \bar{\mathbf{u}}^f + (\nabla \bar{\mathbf{u}}^f)^T)$, where \bar{p}^f represents the filtered fluid pressure, μ^f is the dynamic viscosity of the fluid. The first term in Eq. (1) represents the partial derivative of $\bar{\mathbf{u}}^f$ with respect to time while the ALE referential coordinate $\hat{\mathbf{x}}$ is kept fixed. Based on the formulation in [44], the filtered Navier–Stokes equations (1)–(2) in the weak form can be written as

$$\begin{aligned} \int_{\Omega^f(t)} \rho^f \left(\partial_t \bar{\mathbf{u}}^f + (\bar{\mathbf{u}}^f - \mathbf{w}^f) \cdot \nabla \bar{\mathbf{u}}^f \right) \cdot \boldsymbol{\phi}^f(\mathbf{x}) d\Omega + \int_{\Omega^f(t)} (\bar{\sigma}^f + \sigma^{\text{sgs}}) : \nabla \boldsymbol{\phi}^f(\mathbf{x}) d\Omega \\ = \int_{\Omega^f(t)} \mathbf{b}^f \cdot \boldsymbol{\phi}^f(\mathbf{x}) d\Omega + \int_{\Gamma_h^f(t)} \mathbf{h}^f \cdot \boldsymbol{\phi}^f(\mathbf{x}) d\Gamma, \end{aligned} \quad (3)$$

$$\int_{\Omega^f(t)} \nabla \cdot \bar{\mathbf{u}}^f q(\mathbf{x}) d\Omega = 0. \quad (4)$$

Here ∂_t denotes the partial time derivative operator $\partial(\cdot)/\partial t$, $\boldsymbol{\phi}^f$ and q are the test functions for the fluid velocity and pressure, respectively. $\Gamma_h^f(t)$ represents the non-interface Neumann boundary along which $\sigma^f(\mathbf{x}^f, t) \cdot \mathbf{n}^f = \mathbf{h}^f$, where \mathbf{n}^f is the normal to the fluid boundary. The update of the deformable fluid subdomain is performed by means of the ALE formulation [45,46]. The movement of the internal finite element nodes is achieved by solving a continuum hyperelastic model for the fluid mesh, which maintains the mesh quality as the displacement of the solid increases [47].

2.2. Nonlinear hyperelastic structure

We present the principle of virtual work to express the equations of motion and equilibrium of stresses acting on the structure. The principle of virtual work forms the basis for the finite element method for the dynamics of solids, which will be discussed later in the next section. For a dynamically deforming structure with large strains, we use a nonlinear hyperelastic formulation [48] in the coupled fluid–structure system. Consider a solid with mass density ρ^s that undergoes deformation under external load by fluid flow. Each point on the solid is specified by its position vector. Let $\mathbf{x}^s \in \Omega_0^s$ denote the initial reference position of a point in an undeformed solid, while $\mathbf{d}^s(\mathbf{x}^s, t) \in \Omega^s(t)$ denote the displacement of the point \mathbf{x}^s in the deformed solid after some time t . The function $\boldsymbol{\varphi}^s(\mathbf{x}^s, t) = \mathbf{x}^s + \mathbf{d}^s(\mathbf{x}^s, t)$ is thus a mapping from initial position \mathbf{x}^s to position at time t , which completely specifies the change in the shape of the solid. The velocity field $\mathbf{u}^s(\mathbf{x}^s, t)$, which is defined as $u_i^s(\mathbf{x}_j^s, t) = \frac{\partial \varphi_i^s(\mathbf{x}_j^s, t)}{\partial t}$, describes the motion of the solid under the deformation. The external traction, \mathbf{t}^s is applied on part of the boundary of the solid. We use Γ_2^s to denote the solid boundary that is subjected to external force (Neumann boundary condition) at the reference configuration Ω_0^s , Γ_1^s to denote the rest of the boundary (Dirichlet boundary condition). Both Γ_1^s and Γ_2^s form the boundary Γ^s , such that $\Gamma_1^s \cup \Gamma_2^s = \Gamma^s$. By using the principle of virtual work [48], the following weak form is obtained:

$$\int_{\Omega_0^s} \tau_{ij}^s \delta L_{ij}^s d\Omega - \int_{\Omega_0^s} \rho^s b_i^s \delta v_i^s d\Omega + \int_{\Omega_0^s} \rho^s \frac{\partial u_i^s}{\partial t} \delta v_i^s d\Omega - \int_{\Gamma_2^s} t_i^s \delta v_i^s \eta^s d\Gamma = 0 \quad (5)$$

Here, $\tau_{ij}^s = J^s \sigma_{ij}^s$ is the Kirchhoff stress, $J^s = \det(\mathbf{F}^s)$ is the Jacobian of deformation gradient tensor \mathbf{F}^s ; σ_{ij}^s is the Cauchy stress; $\delta L_{ij}^s = \partial \delta v_i^s / \partial \varphi_j^s$ is the virtual velocity gradients, which satisfies $\delta v_i^s = 0$ along boundary Γ_1^s ; b_i^s is the body force per unit mass, $\delta v_i^s = \delta v_i^s(\mathbf{x}^s)$ is virtual velocity field; η^s is an inverse surface Jacobian which relates the boundary surface of $\Omega^s(t)$ and Ω_0^s as $\eta_{ij}^s = \partial x_i^s / \partial \xi_j$, where ξ_j is the isoparametric coordinate. Note that the usual summation on i, j, k, l is considered in Eq. (5). The Cauchy stress σ_{ij}^s is related to the left Cauchy–Green stress via the neo-Hookean constitutive law as

$$\sigma_{ij}^s = \frac{\mu^s}{(J^s)^{5/3}} (B_{ij}^s - \frac{1}{3} B_{kk}^s \delta_{ij}) + K^s (J^s - 1) \delta_{ij}, \quad \text{with} \quad B_{ij}^s = F_{ik}^s F_{jk}^s \quad (6)$$

where \mathbf{B}^s is the Cauchy–Green tensor, μ^s and K^s are the shear modulus and the bulk modulus of the solid respectively, and the deformation gradient tensor \mathbf{F}^s corresponding to a given displacement field is given as

$$F_{ij}^s = \delta_{ij} + \frac{\partial d_i^s}{\partial x_j}. \quad (7)$$

This completes the description of the hyperelastic structure used in our fluid–structure formulation.

2.3. Interface boundary conditions

Here we present a short description of the coupling interface conditions for the 3D FSI problem which consists of a fluid domain $\Omega^f(t)$, a solid domain $\Omega^s(t)$, and a common interface boundary $\Gamma^{fs}(t) = \partial\Omega^f(t) \cap \partial\Omega^s(t)$. For simplicity we only consider the external load through fluid flow as the solid Neumann boundary, i.e. $\Gamma_2^s = \Gamma^{fs}$. Two interface boundary conditions corresponding to the continuity of tractions and velocities must be satisfied along $\Gamma^{fs}(t)$. Let $\Gamma^{fs} \equiv \partial\Omega^f(0) \cap \partial\Omega_0^s$ be the fluid–solid interface at $t = 0$ and $\Gamma^{fs}(t) = \varphi^s(\Gamma^{fs}, t)$ be the interface at time t . The required conditions to be satisfied are as follows:

$$\bar{\mathbf{u}}^f(\varphi^s(\mathbf{x}^s, t), t) = \mathbf{u}^s(\mathbf{x}^s, t), \quad (8)$$

$$\int_{\varphi^s(\gamma, t)} \boldsymbol{\sigma}^f(\mathbf{x}^f, t) \cdot \mathbf{n} d\Gamma(\mathbf{x}^f) + \int_{\gamma} \mathbf{t}^s d\Gamma = \mathbf{0} \quad (9)$$

where \mathbf{n} is the outer normal to the fluid–body interface, γ is any part of the interface Γ^{fs} in the reference configuration, $d\Gamma$ denotes the differential surface area and $\varphi^s(\gamma, t)$ is the corresponding fluid part at time t . The above conditions are satisfied such that the fluid velocity is exactly equal to the velocity of the body along the interface. The motion of the flexible body is governed by the fluid forces which include the integration of pressure and shear stress effects on the body surface.

3. Partitioned variational fluid–structure system

For the sake of completeness, we next present the discretization using a stabilized variational procedure with equal order interpolations for velocity and pressure. The coupled equations are presented in the semi-discrete variational form for the turbulent fluid flow interacting with a large deformation hyperelastic solid. For a partitioned treatment of the coupled fluid–structure interaction problems, the coupled system is independently discretized with the aid of suitable and desired types of formulations for fluid and structural subdomains, the interface conditions associated with the force equilibrium and no-slip conditions.

3.1. Petrov–Galerkin variational formulation for fluid flow

By means of finite element method, the fluid spatial domain Ω^f is discretized into several non-overlapping finite elements Ω^e , $e = 1, 2, \dots, n_{el}$, where n_{el} is the total number of elements. In this paper, we adopt a generalized- α method to integrate in time $t \in [t^n, t^{n+1}]$, which can be unconditionally stable as well as second-order accurate for linear problems simultaneously. The method enables user-controlled high frequency damping, which is desirable and useful for a coarser discretization in space and time. This method is implemented by means of a single parameter called the spectral radius ρ_∞ which is able to dampen the spurious high-frequency responses and retain the second-order accuracy. With the aid of the generalized- α parameters (α^f, α_m^f) , the expressions employed in the variational form for the flow equation are given as [49]:

$$\bar{\mathbf{u}}_h^{f, n+1} = \bar{\mathbf{u}}_h^{f, n} + \Delta t \partial_t \bar{\mathbf{u}}_h^{f, n} + \gamma^f \Delta t (\partial_t \bar{\mathbf{u}}_h^{f, n+1} - \partial_t \bar{\mathbf{u}}_h^{f, n}), \quad (10)$$

$$\bar{\mathbf{u}}_h^{f, n+\alpha^f} = \bar{\mathbf{u}}_h^{f, n} + \alpha^f (\bar{\mathbf{u}}_h^{f, n+1} - \bar{\mathbf{u}}_h^{f, n}), \quad (11)$$

$$\partial_t \bar{\mathbf{u}}_h^{f, n+\alpha_m^f} = \partial_t \bar{\mathbf{u}}_h^{f, n} + \alpha_m^f (\partial_t \bar{\mathbf{u}}_h^{f, n+1} - \partial_t \bar{\mathbf{u}}_h^{f, n}) \quad (12)$$

where

$$\alpha_m^f = \frac{1}{2} \left(\frac{3 - \rho_\infty^f}{1 + \rho_\infty^f} \right), \quad \alpha^f = \frac{1}{1 + \rho_\infty^f}, \quad \gamma^f = \frac{1}{2} + \alpha_m^f - \alpha^f. \quad (13)$$

Let the space of the trial solutions be denoted by \mathcal{S}^h and the space of test functions be \mathcal{V}^h . The variational form of the flow equations can be written as: find $[\bar{\mathbf{u}}_h^{f, n+\alpha^f}, \bar{p}_h^{n+1}] \in \mathcal{S}^h$ such that $\forall [\boldsymbol{\phi}^f, q] \in \mathcal{V}^h$:

$$\begin{aligned} & \int_{\Omega_h^f} \rho^f \left(\partial_t \bar{\mathbf{u}}_h^{f, n+\alpha_m^f} + (\bar{\mathbf{u}}_h^{f, n+\alpha^f} - \mathbf{w}_h^{f, n+\alpha^f}) \cdot \nabla \bar{\mathbf{u}}_h^{f, n+\alpha^f} \right) \cdot \boldsymbol{\phi}^f d\Omega \\ & + \int_{\Omega_h^f} (\bar{\boldsymbol{\sigma}}_h^{f, n+\alpha^f} + \boldsymbol{\sigma}_h^{sgs, n+\alpha^f}) : \nabla \boldsymbol{\phi}^f d\Omega - \int_{\Omega_h^f} \nabla \cdot \bar{\mathbf{u}}_h^{f, n+\alpha^f} q d\Omega \\ & + \sum_{e=1}^{n_{el}} \int_{\Omega^e} \tau_m^f \left(\rho^f (\bar{\mathbf{u}}_h^{f, n+\alpha^f} - \mathbf{w}_h^{f, n+\alpha^f}) \cdot \nabla \boldsymbol{\phi}^f + \nabla q \right) \cdot \left(\rho^f \partial_t \bar{\mathbf{u}}_h^{f, n+\alpha_m^f} \right. \end{aligned}$$

$$\begin{aligned}
& + \rho^f (\bar{\mathbf{u}}_h^{f,n+\alpha^f} - \mathbf{w}_h^{f,n+\alpha^f}) \cdot \nabla \bar{\mathbf{u}}_h^{f,n+\alpha^f} - \nabla \cdot \bar{\boldsymbol{\sigma}}_h^{f,n+\alpha^f} - \nabla \cdot \boldsymbol{\sigma}_h^{\text{sgs},n+\alpha^f} - \mathbf{b}^f(t^{n+\alpha^f}) \big) d\Omega^e \\
& + \sum_{e=1}^{n_{el}} \int_{\Omega_e} \nabla \cdot \boldsymbol{\phi}^f \tau_c^f \rho^f \nabla \cdot \bar{\mathbf{u}}_h^{f,n+\alpha^f} d\Omega^e \\
& = \int_{\Omega_h^f} \mathbf{b}^f(t^{n+\alpha^f}) \cdot \boldsymbol{\phi}^f d\Omega + \int_{\Gamma_h^f} \mathbf{h}^f \cdot \boldsymbol{\phi}^f d\Gamma,
\end{aligned} \tag{14}$$

where the lines 3, 4 and 5 represent the stabilization terms applied on each element locally. The remaining terms and the right-hand side constitute the Galerkin terms. The stabilization parameters τ_m^f and τ_c^f appearing in the element level integrals are the least-squares metrics, which are added to the fully discretized formulation [50]. The least-squares metric τ_m^f for the momentum equation is defined as:

$$\tau_m^f = \left[\left(\frac{2\rho^f}{\Delta t} \right)^2 + (\rho^f)^2 (\bar{\mathbf{u}}_h^f - \mathbf{w}_h^f) \cdot \mathbf{G} (\bar{\mathbf{u}}_h^f - \mathbf{w}_h^f) + C_I (\mu^f + \mu^t)^2 \mathbf{G} : \mathbf{G} \right]^{-\frac{1}{2}}, \tag{15}$$

where C_I is the constant coming from the element-wise inverse estimate, \mathbf{G} is the size of element contravariant metric tensor and μ^t is the turbulence viscosity. The contravariant metric and the least-squares metric τ_c^f are defined as:

$$\mathbf{G} = \frac{\partial \boldsymbol{\xi}^T}{\partial \mathbf{x}^f} \frac{\partial \boldsymbol{\xi}}{\partial \mathbf{x}^f}, \quad \tau_c^f = \frac{1}{(\text{tr} \mathbf{G}) \tau_m^f}, \tag{16}$$

where \mathbf{x}^f and $\boldsymbol{\xi}$ are the space coordinate and its parametric counterpart respectively and $\text{tr} \mathbf{G}$ denotes the trace of the contravariant metric tensor. The element metric tensor \mathbf{G} intrinsically deals with different element topology for different mesh discretizations. It is worth mentioning that there can be complex interplays between the aforementioned stabilization terms and the effects of subgrid filtering on unresolved mesh for turbulent flow regime. A rigorous mathematical and numerical investigation of this interplay is beyond the scope of this paper.

Linearization of the variational form is carried out by Newton–Raphson technique. Let $\Delta \bar{\mathbf{u}}^f$ and $\Delta \bar{p}^f$ denote the increment in the velocity and pressure variables. The linearized matrix form of Eq. (14) is written as:

$$\mathbf{M}^f \Delta \bar{\mathbf{u}}^f + \theta^f \mathbf{K}^f \Delta \bar{\mathbf{u}}^f + \theta^f \mathbf{N}^f \Delta \bar{\mathbf{u}}^f + \theta \mathbf{G} \Delta \bar{p}^f = \mathbf{R}_m \tag{17}$$

$$-(\mathbf{G}_M^f)^T \Delta \bar{\mathbf{u}}^f - (\mathbf{G}_K^f)^T \Delta \bar{\mathbf{u}}^f + \mathbf{C}^f \Delta \bar{p}^f = R_c \tag{18}$$

where \mathbf{M}^f is the mass matrix, \mathbf{K}^f is the diffusion matrix, \mathbf{N}^f is the convection matrix, \mathbf{G}^f is the pressure gradient operator. \mathbf{G}_M^f , \mathbf{G}_K^f , and \mathbf{C}^f are the contribution of mass matrix, stiffness matrix and pressure matrix for the continuity equation respectively. $\theta^f = 2\Delta t(1 + \rho_\infty^f)/(3 - \rho_\infty^f)$ is a scalar, in which ρ_∞^f is the spectral radius that acts as a parameter to control the high frequency damping [44]. \mathbf{R}_m and R_c are the right hand residual vectors in the linearized form for the momentum and continuity equations, respectively.

3.2. Galerkin variational discretization for hyperelastic structure

Using the principle of virtual work in Eq. (5), we present the finite element approximation for large structural deformations. Without the loss of generality, we consider a hyperelastic material for the structure [51]. The system of structural equations is solved employing the standard Galerkin finite element technique through isoparametric elements for curved boundaries. For an element with n nodes, we denote the coordinates of each node by x_i^a , where the superscript a is an integer ranging from 1 to n , the subscript i is an integer ranging from 1 to 3. The displacement vector at each nodal point will be denoted by $d_i^{s,a}$. The displacement field and virtual velocity field at an arbitrary point within the solid is specified by interpolating between the nodal values as

$$d_i^s(\mathbf{x}^s) = \sum_{a=1}^n N^a(\mathbf{x}^s) d_i^{s,a}, \quad \delta v_i^s(\mathbf{x}^s) = \sum_{a=1}^n N^a(\mathbf{x}^s) \delta v_i^{s,a}, \tag{19}$$

where \mathbf{x}^s denotes the coordinates of an arbitrary solid point in the reference configuration and N^a denotes the shape function. By substituting the appropriate deformation measure, the Kirchhoff stress can be calculated. Note that the Kirchhoff stress depends on the displacements through the deformation gradient. Substituting Eq. (19) into the virtual work equation, we obtain the following variational equation for nonlinear structure:

$$\int_{\Omega_0^s} \rho^s N^b N^a \frac{\partial^2 d_i^{s,b}}{\partial t^2} d\Omega + \int_{\Omega_0^s} \tau_{ij}^s [F_{pq}^s(d_i^{s,a})] \frac{\partial N^a}{\partial x_m} F_{mj}^{s,-1} d\Omega - \int_{\Omega_0^s} \rho^s b_i^s N^a d\Omega - \int_{\Gamma^{fs}} t_i^s N^a \eta^s d\Gamma = 0. \quad (20)$$

The volume and surface integrals in the above virtual work equation are taken over the reference configuration. Using the inverse surface Jacobian η^s the deformed configuration is mapped back to the reference configuration. The virtual work Eq. (20) gives a set of n nonlinear equations with n unknowns due to the geometric terms associated with the finite deformations. Notably $\tau_{ij}^s[F_{pq}^s(d_i^{s,a})]$ is a functional relationship, which relates the Kirchhoff stress through the deformation gradient. This nonlinear virtual work equation is solved by means of Newton–Raphson iteration within each time step. We next briefly summarize the linearization process to construct a linear system of equations.

Let the correction of the displacement vector be $\Delta \mathbf{d}^s$. After linearizing the virtual work equation Eq. (20) with respect to $\Delta \mathbf{d}^s$, we have the following system of linear equations:

$$\mathbf{M}^s \Delta \ddot{\mathbf{d}}^s + \mathbf{K}^s \Delta \mathbf{d}^s = \mathbf{R}_s \quad (21)$$

where \mathbf{M}^s is the finite element mass matrix, \mathbf{K}^s is the finite element stiffness matrix, and the net force vector \mathbf{R}_s , which consists of the external force and the residual terms. The expressions for the mass matrix \mathbf{M}^s and the stiffness matrix \mathbf{K}^s are given by

$$M_{ab}^s = \int_{\Omega_0^s} \rho^s N^b N^a d\Omega \quad (22)$$

$$K_{aibk}^s = \int_{\Omega_0^s} \frac{\partial \tau_{ij}^s}{\partial F_{kl}^s} \frac{\partial N^b}{\partial x_l} \frac{\partial N^a}{\partial x_m} F_{mj}^{s,-1} d\Omega - \int_{\Omega_0^s} \tau_{ij}^s \frac{\partial N^a}{\partial x_m} F_{mk}^{s,-1} \frac{\partial N^b}{\partial x_p} F_{pj}^{s,-1} d\Omega - \int_{\Gamma^{fs}} t_i^s N^a \frac{\partial \eta^s}{\partial d_k^{s,b}} d\Gamma, \quad (23)$$

whereas the net force vectors \mathbf{R}_s is as follows

$$\{\mathbf{R}_s\}_i^a = \int_{\Omega_0^s} \rho^s b_i^s N^a d\Omega - \int_{\Omega_0^s} \rho^s N^b N^a \frac{\partial^2 d_i^{s,b}}{\partial t^2} d\Omega - \int_{\Omega_0^s} \tau_{ij}^s \frac{\partial N^a}{\partial x_m} F_{mj}^{s,-1} d\Omega + \underbrace{\int_{\Gamma^{fs}} t_i^s N^a \eta^s d\Gamma}_{\text{External fluid force, } \mathbf{f}^s}. \quad (24)$$

Through the inverse surface Jacobian η^s , we can relate the nominal \mathbf{t}_0^s and true traction \mathbf{t}^s as $\mathbf{t}_0^s = \eta^s \mathbf{t}^s$ on the reference boundary Γ^{fs} . After the current time step solution is obtained, we integrate these equations with respect to time to update the solution in time. For our fluid–structure problems, we consider implicit Newmark time integration method to handle this dynamical nonlinear system. The stiffness matrix is rebuilt at each iteration within a time step. In the spirit of partitioned treatment and domain decomposition, the fluid and solid subdomains are solved iteratively. We next present the coupled fluid–structure matrix formulation and the iterative force correction procedure.

3.3. Nonlinear iterative force correction scheme

In this section, we present the coupled matrix form of the variational finite element equations defined in the previous subsection at the semi-discrete level for non-overlapping decomposition of two subdomains of fluid and structure. A variational problem of fluid–structure system discretized by a finite element method gives a coupled linear system of equations with the unknowns of fluid and structure in the form $\mathbf{A}\mathbf{u} = \mathbf{R}$, where \mathbf{R} is a given right-hand side and \mathbf{u} is the vector of unknowns for the fluid–structure system. Corresponding to the domain decomposition, the set of degrees of freedom (DOF) is decomposed into interior DOFs for the fluid–structure system and interface DOFs for the Dirichlet-to-Neumann (DtN) map. Using the coupled fluid–structure Eqs. (17), (18), (21) and the Dirichlet-to-Neumann map along the interface, the resultant block decomposition of the linear system can be expressed in the following abstract form:

$$\begin{bmatrix} \mathbf{A}_{ss} & \mathbf{0} & \mathbf{0} & \mathbf{A}_{fs} \\ \mathbf{A}_{ds} & \mathbf{I} & \mathbf{0} & \mathbf{0} \\ \mathbf{0} & \mathbf{A}_{dq} & \mathbf{A}_{qq} & \mathbf{0} \\ \mathbf{0} & \mathbf{0} & \mathbf{A}_{fq} & \mathbf{A}_{ff} \end{bmatrix} \begin{bmatrix} \Delta \mathbf{d}^s \\ \Delta \mathbf{d}^l \\ \Delta \mathbf{q}^f \\ \Delta \mathbf{f}^l \end{bmatrix} = \begin{bmatrix} \mathbf{R}_s \\ \mathbf{R}_l^D \\ \mathbf{R}_q^N \\ \mathbf{R}_l^N \end{bmatrix} \quad (25)$$

where \mathbf{d}^s is the structural displacement, $\mathbf{q}^f = (\bar{\mathbf{u}}^f, \bar{\mathbf{p}}^f)$ denotes the fluid unknown variables, \mathbf{d}^l and \mathbf{f}^l are the displacement and force along the coupling interface. On the other side, \mathbf{R}_s and $\mathbf{R}_q = (\mathbf{R}_m, \mathbf{R}_c)$ are the right hand side of the corresponding solid and fluid equations; \mathbf{R}_l^D and \mathbf{R}_l^N are the residual errors representing the imbalances during the enforcement of the Dirichlet (kinematic) condition and Neumann (dynamic) condition between the non-overlapping decomposed fluid and solid subdomains. The left-hand side matrix \mathbf{A} represents the derivatives of the fluid, solid, interface equations with respect

to their state variables. The subscripts s, q denote the interior DOFs for the solid and fluid and d, f represent the interface DOFs for the displacement and force. While the block matrix \mathbf{A}_{ss} corresponds to the mass and stiffness matrix of the structure in Eq. (21), \mathbf{A}_{qq} corresponds to the coupled fluid velocity and pressure linear system in Eq. (17) and (18). \mathbf{A}_{ds} is an extraction matrix which maps the solid displacement to the interface, \mathbf{A}_{df} is a matrix which relates the displacement of the interface to the fluid through ALE. \mathbf{A}_{fq} is the computation of the force and its mapping to the interface. \mathbf{A}_{fs} is a matrix that gets the solid load vector from the fluid–solid interface force. During the partitioned Dirichlet-to-Neumann coupling, there is no explicit availability of the Jacobian matrix \mathbf{A}_{fs} entered in the coupled fluid–structure system Eq. (25).

By eliminating the off-diagonal term \mathbf{A}_{fs} in Eq. (25) via static condensation, we can obtain the following reduced linear system:

$$\begin{bmatrix} \mathbf{A}_{ss} & 0 & 0 & 0 \\ \mathbf{A}_{ds} & \mathbb{I} & 0 & 0 \\ 0 & \mathbf{A}_{dq} & \mathbf{A}_{qq} & 0 \\ 0 & 0 & 0 & \tilde{\mathbf{A}}_{ff} \end{bmatrix} \begin{bmatrix} \Delta \mathbf{d}^s \\ \Delta \mathbf{d}^l \\ \Delta \mathbf{q}^f \\ \Delta \mathbf{f}^l \end{bmatrix} = \begin{bmatrix} \mathcal{R}_s \\ \mathcal{R}_l^D \\ \mathcal{R}_q^N \\ \tilde{\mathcal{R}}_l^N \end{bmatrix} \quad (26)$$

where the derivation and the terms $\tilde{\mathbf{A}}_{ff}$ and $\tilde{\mathcal{R}}_l^N$ are described in detail in [44]. The idea is to compute the iterative correction for the interface fluid force $\mathbf{f}^l = \int_{\Gamma^f} \boldsymbol{\sigma}^f \cdot \mathbf{n} d\Gamma$ over the deformed ALE configuration as the structure moves. In the nonlinear iterative force correction, we construct a force correction vector in the following manner to correct the previous force \mathbf{f}_k^l at k th sub-iteration:

$$\Delta \mathbf{f}^l = \tilde{\mathbf{A}}_{ff}^{-1} \tilde{\mathcal{R}}_l^N \quad (27)$$

Here, the force correction vector $\tilde{\mathbf{A}}_{ff}^{-1} \tilde{\mathcal{R}}_l^N$ at the k th sub-iteration can be constructed by successive approximation, which essentially estimates the coupled effects along the fluid–solid interface. The off-diagonal terms are not explicitly formed and the method instead proceeds in a predictor–corrector format by constructing an iterative interface force correction at each sub-iteration. This iterative force correction relies on the input–output relationship between the displacement and the force transfer at each sub-iteration. When the brute-force sub-iterations lead to severe numerical instabilities during strong added-mass effects, the NIFC-based correction provides stability to the partitioned FSI coupling [44]. The present force correction method can be interpreted as a generalization of Aitken's Δ^2 extrapolation method [52,53] to provide convergent behavior to the interface force sequence generated through the nonlinear iterations between the fluid and the structure. The geometric extrapolation with the aid of dynamic weighting parameter allows transforming a divergent fixed-point iteration to a stable and convergent iteration [44,23]. We next present the common-refinement method to transfer the fluid traction over the solid boundary across non-matching meshes.

4. 3D common-refinement method

In this section, we will address the central topic of this paper focusing on the spatial coupling between the fluid and the structure for non-matching meshes via common-refinement. The fluid and the structural equations are coupled by the continuity of velocity and traction along the fluid–solid interface. We consider that the fluid–structure boundary is discretized independently by the same polynomial order of shape functions for both fluid and solid subdomains. During the ALE updates, the deformed fluid subdomain using isoparametric elements follows the deformed structure and the discrete fluid and solid meshes remain coincident to the physical fluid–structure boundary.

4.1. Variational interface condition

To satisfy the traction equilibrium condition, the momentum flux from the fluid flow must be transferred to the structural surface through the surface traction. To formulate the load transfer operator for the common-refinement method, the weighted residual based on ℓ_2 minimization is considered. Let N_i^f and N_j^s denote the standard finite element shape functions associated with node i of the fluid and node j of the solid interface meshes respectively, while $\tilde{\mathbf{t}}_i^f \in L^2(\Omega^f)$ and $\tilde{\mathbf{t}}_j^s \in L^2(\Omega^s)$ denote the approximate nominal tractions at the corresponding nodes of the discrete fluid interface Γ_h^f and solid interface Γ_h^s respectively. The continuum traction fields \mathbf{t}^f and \mathbf{t}^s over Γ^f and Γ^s are interpolated as follows:

$$\mathbf{t}^f(\mathbf{x}^f) \approx \sum_{i=1}^{m_f} N_i^f \tilde{\mathbf{t}}_i^f, \quad \mathbf{t}^s(\mathbf{x}^s) \approx \sum_{j=1}^{m_s} N_j^s \tilde{\mathbf{t}}_j^s, \quad (28)$$

where m_f and m_s are the number of fluid and solid nodes on the fluid and solid interface meshes respectively. Once we have \mathbf{t}^f , N_i^f , and N_j^s , we can obtain the transferred distributed loads by solving for $\tilde{\mathbf{t}}_j^s$. We can measure the residual $\mathbf{t}^s - \mathbf{t}^f$, by minimizing the ℓ_2 norm employing the Galerkin weighted residual method. Multiplying both sides with a set of weighting functions ($W_i = N_i^s$), and integrating over the interface boundary Γ^{fs} , we obtain:

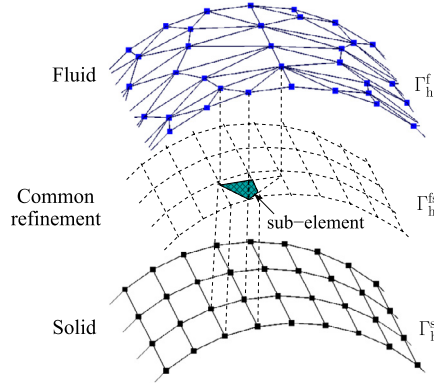


Fig. 1. Schematic of common-refinement based projection method for load transfer in 3D; where shaded area denotes one surface sub-element. Physical fluid–solid interface has two realizations of fluid and solid sides.

$$\int_{\Gamma^{fs}} N_i^s \mathbf{t}^s d\Gamma = \int_{\Gamma^{fs}} N_i^f \mathbf{t}^f d\Gamma. \quad (29)$$

Note that, by satisfying Eq. (29), the momentum is conserved in the weak sense across the fluid–solid interface. Owing to the weighted residual formulation and the partition of unity of the shape function, the global discrete conservation is achieved by construction for the integrals in Eq. (29). Next using finite element approximations of fluid and solid tractions, the traction equilibrium condition is written as:

$$\int_{\Gamma^{fs}} N_i^s N_j^s \tilde{\mathbf{t}}_j^s d\Gamma = \int_{\Gamma^{fs}} N_i^f N_j^f \tilde{\mathbf{t}}_j^f d\Gamma, \quad (30)$$

which gives solid-side tractions $\tilde{\mathbf{t}}_j^s$ as

$$\tilde{\mathbf{t}}_j^s = [M_{ij}^s]^{-1} \{f_i^s\}, \quad (31)$$

where $[M^s]$ represents the mass matrix for the solid interface elements and is defined by:

$$[M_{ij}^s] = \int_{\Gamma^{fs}} N_i^s N_j^s d\Gamma, \quad (32)$$

and $\{f_j^s\}$ is the nodal force vector given as:

$$\{f_i^s\} = \sum_{j=1}^{m_f} \tilde{\mathbf{t}}_j^f \int_{\Gamma^{fs}} N_i^f N_j^f d\Gamma. \quad (33)$$

This completes the general formulation of the weighted residual method for extracting the load vector on the solid side interface. While the construction of mass matrix requires only the solid side shape functions, the load vector integral consists of shape functions from both the fluid and the solid sides. For matching grids, this would not cause any problem. However, for non-matching grids, the inconsistency of shape functions will lead to integrations across discontinuities. To resolve this issue, there is a need for the common-refinement surface which allows to perform integrations consistently. Further details of common-refinement construction for three-dimensional surface meshes can be found in [37]. While the energy conservation property of the common-refinement has been analyzed in [34], the relevance of consistent load transfer on the energy conservation in the context of the current formulation has been presented in Appendix A.

4.2. Algorithmic details

The common-refinement method is a special data structure for transferring data between meshes that have varying degrees of mesh mismatch. As shown in Fig. 1, the common-refinement surface of two meshes consists of polygons that subdivide the input boundary meshes of fluid and solid subdomains simultaneously. Every sub-element of a common-refinement mesh has two geometrical realizations, in general, which are different but must be close to each other to obtain a physically consistent data transfer. In the finite element form, the spatial configuration of the fluid and solid interface meshes can be written as:

$$\mathbf{x}^f \approx \sum_{i=1}^{m_f} N_i^f(\mathbf{x}) \tilde{\mathbf{x}}_i^f \text{ on } \Gamma_h^f, \quad \mathbf{x}^s \approx \sum_{j=1}^{m_s} N_j^s(\mathbf{x}) \tilde{\mathbf{x}}_j^s \text{ on } \Gamma_h^s. \quad (34)$$

Within this paper, the topology of the common-refinement sub-elements are defined by the intersection of the surface elements of input meshes. These 3D sub-elements are illustrated in Fig. 1. We notice that the intersection of two arbitrary triangles or two hybrid surface elements can be quite complex.

During FSI simulation, within the common-refinement method, the load vector f_j^s over the common-refinement mesh nodes is computed as follows:

$$f_j^s = \sum_{i=1}^{e_c} \int_{\sigma_i^c} N_j^s \tilde{\mathbf{t}}^f d\Gamma, \quad (35)$$

where e_c represents the total number of sub-elements of the common-refinement overlay surface, and σ_i^c represents its i th sub-element. We use the Gaussian integration to determine the integration point locations and their weight functions. The basic steps of CRM are summarized in Algorithm 1.

Algorithm 1 3D common-refinement method.

1. Collect input meshes and construct common-refinement sub-elements
 2. Loop over defined sub-elements over fluid interface Γ_h^f
 - (a) Loop over quadrature points of the sub-elements
 - (b) Calculate sub-element area over fluid interface
 - (c) Associate quadrature points onto corresponding solid element
 - (d) Integrate traction vectors via common-refinement sub-elements
 - (e) Compute solid load vector integral using Eq. (35)
-

4.3. Common-refinement with NIFC scheme

In this section, we summarize the partitioned iterative coupling of the ALE fluid-turbulence solver with the hyperelastic structure solver, as illustrated in Fig. 2. The solution to the hyperelastic structure equations provides a predictor displacement. The ALE fluid equations with turbulence are then solved to evaluate and correct the forces at the fluid–solid interface. Let the structural displacement be denoted by $\mathbf{d}^s(\mathbf{x}^s, t^n)$ due to the turbulent fluid forces at time t^n . The first step of the iterative procedure at iteration k involves the prediction of the displacement of the hyperelastic structure due to the fluid forces. The computed structural displacements are then transferred to the fluid side by satisfying the ALE compatibility and the velocity continuity conditions at the interface Γ^{fs} in the second step. This is elaborated as follows: suppose $\mathbf{d}^{m,n+1}$ is the mesh displacement at time t^{n+1} . The mesh displacements are equated to the structural displacements at the fluid–solid interface to avoid any gaps and overlaps between the non-matching fluid and solid mesh configurations

$$\mathbf{d}^{m,n+1} = \mathbf{d}^s \quad \text{on } \Gamma^{fs}. \quad (36)$$

The fluid velocity is then equated with the mesh velocity to satisfy the velocity continuity on Γ^{fs} as

$$\tilde{\mathbf{u}}^{f,n+\alpha^f} = \mathbf{w}^{f,n+\alpha^f} = \frac{\mathbf{d}^{m,n+1} - \mathbf{d}^{m,n}}{\Delta t} \quad \text{on } \Gamma^{fs}. \quad (37)$$

In the third step of the iteration k , the ALE Navier–Stokes equations with subgrid LES filtering are solved at the mid-point moving mesh configuration to evaluate the fluid forces. The computed forces are finally corrected using the NIFC filter and transferred to the hyperelastic structural solver in the fourth step of the nonlinear iteration. When the solver has achieved the convergence criteria, the fluid–structure solver is advanced in time after updating the variable values at t^{n+1} .

In this numerical study, we employ the Newton–Raphson technique to minimize the linearization error at each time step and the flow and the ALE mesh fields are updated in time by the generalized- α method [49]. The resulting incremental velocity, pressure and mesh displacement coming from the finite element discretization are evaluated by solving the linear system of equations via the Generalized Minimal RESidual (GMRES) algorithm proposed in [54], which relies on the Krylov subspace iteration and the modified Gram–Schmidt orthogonalization. Note that to solve the linear matrix system, we do not explicitly form the left hand-side matrix, rather we perform the needed matrix-vector product of each block matrix in pieces for the GMRES algorithm. The solver relies on hybrid parallelism for the solution of partitioned NIFC-based FSI solver for parallel computing. The parallelization employs a standard master-slave strategy for distributed memory clusters via message passing interface (MPI) based on a domain decomposition strategy. The master process extracts the mesh and generates the partition of the mesh into subgrids via an automatic graph partitioner. Each master process performs the computation for the root subgrid and the remaining subgrids behave as the slaves [55,56]. While the local element matrices

Table 1
Dependence of load vector error ϵ_1 on different mesh ratios h_s/h_f .

N_s	N_f	A_s/A_f	Error, ϵ_1
36	216	6.0	2.94896×10^{-3}
36	162	4.5	2.88308×10^{-3}
36	108	3.0	2.69495×10^{-3}
36	54	1.5	1.6836×10^{-6}
36	36	1.0	2.51×10^{-16}
54	36	0.6667	1.76919×10^{-6}
108	36	0.3333	3.30083×10^{-3}
162	36	0.2222	3.29819×10^{-3}
216	36	0.1667	3.32599×10^{-3}

Without the loss of generality, we choose $w_z = 36$ in our numerical analysis. In addition, the physical surface is discretized into N_s and N_f elements along the circumference of the cylinder. The resultant number of elements on the fluid and the solid surfaces is $w_z N_f$ and $w_z N_s$, respectively. The distributions of element sizes are uniform along each surface. Fig. 3b shows a typical patch of the non-matching fluid and the solid surface meshes. We define the size of the element on each surface through the area of each element as follows:

$$A_s = \frac{\pi D H}{w_z N_s}, \quad A_f = \frac{\pi D H}{w_z N_f}. \quad (38)$$

The degree of non-matching is quantified by using the mesh ratio between these two surfaces, A_s/A_f . Several meshes with different mesh sizes are generated by setting $N_s, N_f \in \{36, 54, 108, 162, 216\}$. Consequently, this leads to the mesh ratio of $A_s/A_f \in [1/6, 6]$. For each set of these meshes, a prescribed load is applied on the node of fluid surface mesh at position \mathbf{x}^f and is transferred to the solid surface via the common-refinement method. Consider the prescribed loading function in the following form:

$$\mathbf{t}^s = \mathbf{t}^s(\theta, z) = - \left(\frac{1}{2} \rho^f U_\infty^2 (1 - 4 \sin^2 \theta) + \rho^f g z \right) \begin{pmatrix} 0.5 \cos \theta \\ 0.5 \sin \theta \\ 0 \end{pmatrix} \quad (39)$$

where $(\theta, z) \in \Gamma^{fs}$ is the cylindrical position vector on the surface of the cylinder and $U_\infty = 1$. Note that the origin of the cylindrical coordinates lies at the center of the top surface of the cylinder, as shown in Fig. 3a. The prescribed load in Eq. (39) is generated through the estimation of static pressure along Z -direction from the potential flow around a cylinder. Let (θ_j^s, z_j^s) be the position vector of node j on the solid surface, \mathbf{T}_j^s be the load vector transferred to the solid node, and $\|\cdot\|_2$ be the ℓ_2 norm, the relative error ϵ_1 is defined as

$$\epsilon_1 = \frac{\sum_j \|\mathbf{T}_j^s - \mathbf{t}^s(\theta_j^s, z_j^s)\|_2}{\sum_j \|\mathbf{t}^s(\theta_j^s, z_j^s)\|_2}. \quad (40)$$

Table 1 shows the relative error ϵ_1 computed for the mesh ratio ranging from 0.1667 to 6.0. The error analysis shows that the common-refinement method performs well within the interpolation error for all the mesh ratios. More importantly, it is worth noting that the error is consistent for both $h_s/h_f > 1$ and $h_s/h_f < 1$. This is expected as the overlay surface constructed in the common-refinement method involves both the fluid and the solid meshes.

To further quantify the error of our common-refinement method, we choose $h_s/h_f = 1.5$ and $h_s/h_f = 0.6667$ as the reference mesh ratios for the spatial convergence study. For each mesh ratio, we increase both N_s and N_f simultaneously by maintaining the mesh ratio while lowering the error introduced due to the underlying spatial discretization. The relative error ϵ_1 in the standard discrete least-square norm for the non-matching meshes is shown in Fig. 4. It is found that the gradient of the error trend is two, which implies that the common-refinement method is optimally accurate up to the geometric interpolation.

A further capability of our common-refinement method in handling surface meshes with different shapes is also demonstrated by transferring the data from a triangular mesh to a quadrilateral mesh. The setup of the data transfer is identical to the one shown in Fig. 3a, except that the fluid surface is now discretized via triangular elements, while the solid surface is decomposed by quadrilateral elements. The traction on the fluid is prescribed by Eq. (39), and the error of the data transfer is computed by Eq. (40). Different mesh sizes, h ranged from 0.04 to 0.2 are tested, and their errors are shown in Fig. 5. It is found that the common-refinement method maintains a second order accuracy in transferring loads between meshes with different shapes.

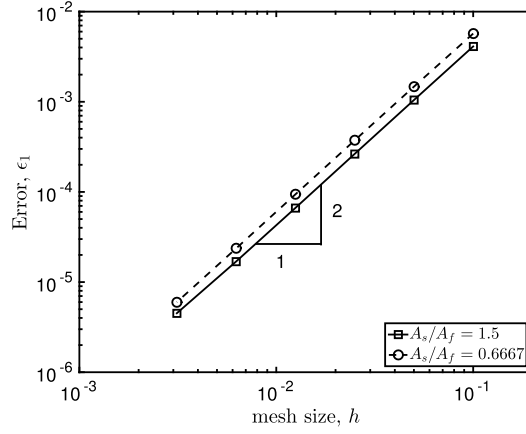


Fig. 4. Spatial mesh convergence study of common-refinement method for non-matching meshes.

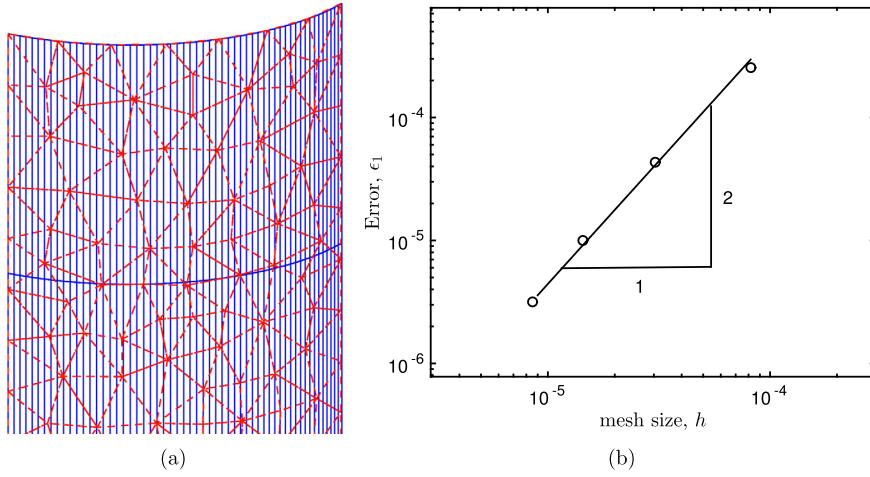


Fig. 5. Demonstration of common-refinement method for triangular-to-quadrilateral data transfer: (a) the representative surface meshes, and (b) the spatial error ϵ_1 versus mesh size h .

5.2. Transient data transfer

We next analyze the second type of numerical error, which is introduced during the repeated transfer of interface data across non-matching meshes. This numerical analysis is performed by considering a long deformable cylinder in a flowing channel for the meshes with different degrees of mismatches along the wetted fluid–solid boundary. The schematic diagram of the problem setup is shown in Fig. 6a. The cylinder is modeled as an elastic tube with spanwise length of $50D$. Both of its ends are fixed at Γ_{top} and Γ_{bottom} . A free-stream flow velocity of $u^f = U$ is specified at Γ_{in} of the computational domain where u^f is the X-component of the fluid velocity $\vec{u}^f = (u^f, v^f, w^f)$, while the traction-free boundary condition is considered at Γ_{out} . A slip boundary condition is applied on Γ_{top} and Γ_{bottom} , and the no-slip boundary condition is imposed on the surface of the cylinder. The cylinder is placed $10D$ away from the inlet boundary Γ_{in} , while it is $30D$ away from Γ_{out} .

The data transfer occurs at the surface of the flexible cylinder, where the traction of the fluid is transferred to the solid domain. Likewise, the static data transfer, both the fluid and the solid surfaces are discretized into w_θ elements along the circumference and w_z elements along the spanwise direction. As a representative case, we choose $w_\theta = 32$ and $w_z = 25$ in this analysis. This leads to a mesh ratio of $A_s/A_f = 1$, where the areas of fluid and solid element are identical. A mismatch between both surfaces is then generated by fixing the fluid mesh and having a rotation of the solid mesh along the spanwise axis of the cylinder. Fig. 6b shows a schematic diagram for such kind of mismatch of the meshes for the fluid and the solid subdomains. For each fluid surface element k and the solid element j , there is a corresponding sub-element on the common-refinement surface. The sub-element is the intersection of the projected elements of both subdomains. Let $A_{k,j}$ be the area of the sub-element corresponding to the fluid surface element k and the solid surface element j , the degree of mismatch with respect to the fluid element k , which is termed as $\delta_k^{F \rightarrow S}$ is defined as follows

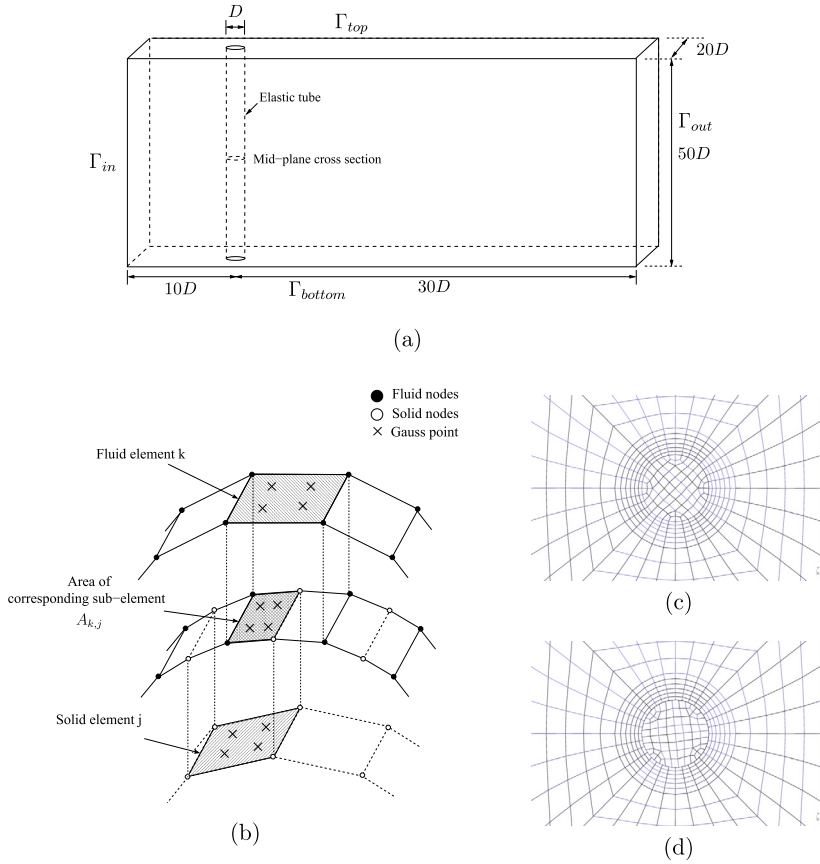


Fig. 6. Computational setup for the transient analysis of common-refinement discretization: (a) schematic diagram of physical setup for the deformable tube problem in a uniform flow; (b) sketch of non-matching meshes and their projected area on the common-refinement surface; (c) and (d) show the meshes on the mid-plane cross section for matching ($\delta_{F \rightarrow S} = 0$) and non-matching ($\delta_{F \rightarrow S} = 0.5$) scenarios.

$$\delta_k^{F \rightarrow S} = \left(1 - \frac{\max_j A_{k,j}}{\sum_j A_{k,j}} \right). \quad (41)$$

The degree of mismatch with respect to the fluid surface $\delta^{F \rightarrow S}$ is then defined as the mean degree of the mismatch with respect to each fluid element

$$\delta^{F \rightarrow S} = \frac{1}{N} \sum_{k=1}^N \delta_k^{F \rightarrow S}. \quad (42)$$

With this definition, it is found that $\delta_{F \rightarrow S} \in [0, 0.5]$ in our case, where $\delta_{F \rightarrow S} = 0$ corresponds to the matching mesh, $\delta_{F \rightarrow S} = 0.5$ corresponds to a staggered configuration between the fluid and the solid elements. Five sets of meshes with different degrees of mismatches, including $\delta_{F \rightarrow S} = 0$, are used in the numerical experiments to assess the accuracy of the common-refinement method. The matching mesh is selected as a reference case to evaluate the error associated with the degree of mismatch.

The characteristic responses of the deformable tube are compared between the different mesh configurations. These include the in-line displacement, the cross-flow displacement, the drag coefficient (C_d) and the lift coefficient (C_l). To quantify the effect of degree of mismatch on these physical quantities, we compute the error as follows:

$$\epsilon_2 = \frac{\|\mathbf{R} - \mathbf{R}_{\delta_{F \rightarrow S}=0}\|_{\infty}}{\|\mathbf{R}_{\delta_{F \rightarrow S}=0}\|_{\infty}} \quad (43)$$

where \mathbf{R} is a vector containing the temporal characteristic response from the non-matching mesh, $\mathbf{R}_{\delta_{F \rightarrow S}=0}$ is the corresponding temporal response of the matching mesh and $\|\cdot\|_{\infty}$ is the infinity norm. The error associated with each of the characteristic responses is summarized in Table 2. It can be observed that there is a very small difference between the responses during the simulation. Therefore, it shows that the 3D common-refinement method developed in this work is both reliable and accurate in transferring the data between the fluid and the solid meshes. We next analyze the performance of our implementation of the common-refinement method.

Table 2

The relative error of characteristic response between the matching and non-matching meshes.

$\delta_{F \rightarrow S}$	$x/D(\times 10^{-3})$	$y/D(\times 10^{-3})$	$C_l(\times 10^{-3})$	$C_d(\times 10^{-3})$
0.1	1.2512	2.1213	0.0791	1.2382
0.2	1.6620	3.0710	0.1102	1.5931
0.3	3.6998	3.9819	0.1301	1.6318
0.4	5.6904	4.8199	0.1691	1.8075
0.5	7.5399	5.6292	0.2005	2.1933

Table 3

Average elapsed time for each component in an iteration collected from 500 steps of simulation. The percentage is computed with respect to the average elapsed time for each iteration. The common refinement method implemented has insignificant contribution to the total time spent.

Component	Average elapsed time (s)	Percentage (%)
Fluid	17.82	89.30%
Solid	2.14	10.69%
Common refinement	1.77×10^{-3}	0.01%

5.3. Performance

At each time step, the coupled fluid–structure solver undergoes several nonlinear iterations to correct the interface forces. The elapsed time spent in each iteration consists of three main components, namely the fluid solver, the solid solver, and the common-refinement data transfer. We assess the performance of each component by collecting its time taken for each iteration. Without the loss of generality, the reference case studied in Section 5.2 is considered for the performance assessment. The fluid domain is discretized into 33450 brick elements with 35984 nodes, while the solid domain is discretized into 1800 brick elements with 2314 nodes. The fluid–solid interface consists of 800 quadrilateral elements with 832 nodes. The simulation is then conducted in parallel with dual cores in Intel(R) Xeon(R) CPU E5-2630L v2 @ 2.40 GHz. The elapsed time for each component is collected over 500 time steps, and Table 3 summarizes their average elapsed time for each component in an iteration. On average, there are about four iterations pass through in each time step to satisfy the convergence tolerance of 10^{-5} .

It is observed that the most of the time is spent on both the volumetric (bulk) fluid and the solid computations, while the common-refinement data transfer does not contribute significantly to the total elapsed time. This observation is consistent with the previous finding of [35], where the computational cost of the common-refinement data transfer is found to be insignificant when compared to the overall computation cost. We further assess the performance by investigating the parallel implementation of the common-refinement method. For the parallel implementation, the elapsed time is collected for the data transferred across two surfaces using different number of processors. Both fluid and solid surfaces are 100 units long in width and length. The surfaces are discretized into 5040×1000 quadrilateral elements, which accounts to 5041×1001 nodes on each surface. Without the loss of generality, an arbitrary data is assigned to each node on one of the surface and is transferred to the other surface via common-refinement method. In the parallel setup, the meshes will be partitioned according to the number of processors used before the data is transferred. Fig. 7 shows the elapsed time to complete the data transfer from one surface to the other at different number of processors ranging from 2 to 16. The best fitted line in the graph has a negative gradient of one, which indicates that the time taken is inversely proportional to the number of processors. This confirms that the parallel performance of our common-refinement method is scalable to the number of processors. To further assess the stability and accuracy of our 3D fluid–structure solver with non-matching meshes, we next present a standard benchmark problem of an elastic bar attached to a circular cylinder.

6. Three-dimensional FSI with non-matching meshes

Before we proceed to the demonstration of our proposed hybrid CR-NIFC method for non-matching meshes, we first verify our partitioned fluid–structure computation against the available data in the literature. For this purpose, we consider the unsteady cylinder-bar problem (FSI-III) presented in [58] for low structural-to-fluid density ratio and $Re = 200$ based on the diameter of the cylinder. The simulation consists of a thin flexible structure with a finite thickness clamped behind a fixed rigid non-rotating cylinder. The cylinder-bar system is installed in a rectangular fluid domain. A schematic of the cylinder-bar system and computational domain is shown in Fig. 8a. Table 4 summarizes the fluid–structure parameters used for this benchmark problem.

The boundary conditions for this FSI setup are identical to the benchmark case presented in [58]. The no-slip Dirichlet condition is implemented on the surface of the cylinder wall, the flexible bar and on the top and the bottom surfaces. Of particular interest is the fluid–solid interface between the flexible bar and the fluid subdomain. A traction-free condition is implemented on the outlet Γ_{out} . A parabolic velocity profile is specified at Γ_{in} :

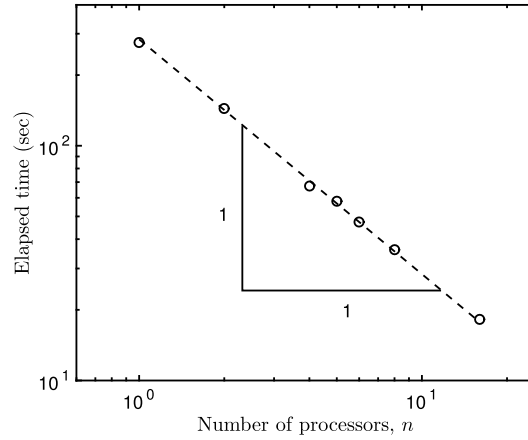
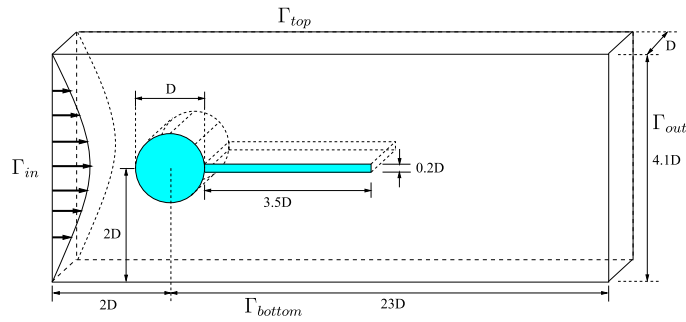
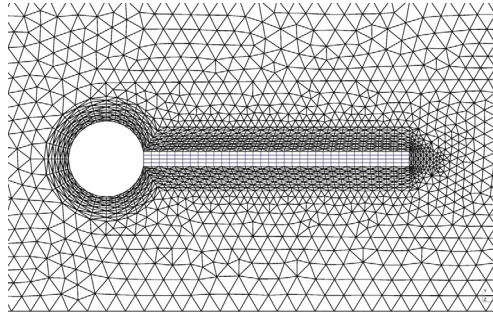


Fig. 7. Parallel performance of the common-refinement method. The number of processors tested ranges from 2 to 16. The dotted line is the best fitted line for data collected, which has a negative gradient of one.



(a) Schematic of unsteady cylinder-bar problem



(b) Representative matching mesh M1

Fig. 8. Unsteady cylinder-bar problem for the verification and convergence study. Details of meshing parameters are listed in Table 4.

Table 4

FSI parameters for unsteady cylinder-bar problem at $Re = 200$ and $\rho^s/\rho^f = 1.0$.

Parameters	Benchmark
Cylinder diameter, D	0.1 m
Mean inlet velocity, \bar{U}	1.0 m/s
Fluid density, ρ^f	1000 kg/m ³
Bar thickness, w	0.02 m
Bar length, L	0.35 m
Structure density, ρ^s	1000 kg/m ³
Young modulus, E	5.6×10^5 Pa
Reynolds number, Re	200
Density ratio, $\rho^f = \frac{\rho^s}{\rho^f}$	1.0
Poisson's ratio, ν^s	0.4

Table 5

Mesh convergence and validation of FSI-III case. The percentage differences are calculated by using M3 result as the reference.

Mesh	Fluid elements	Solid elements	$A_{x,max}$	$A_{y,max}$	f_y
M1	7171	136	2.68 (9.39%)	32.94 (0.15%)	5.15 (4.90%)
M2	11770	544	2.55 (4.08%)	31.89 (3.04%)	5.34 (1.34%)
M3	25882	1280	2.45	32.89	5.42
Benchmark	9216	1280	2.68	35.34	5.3

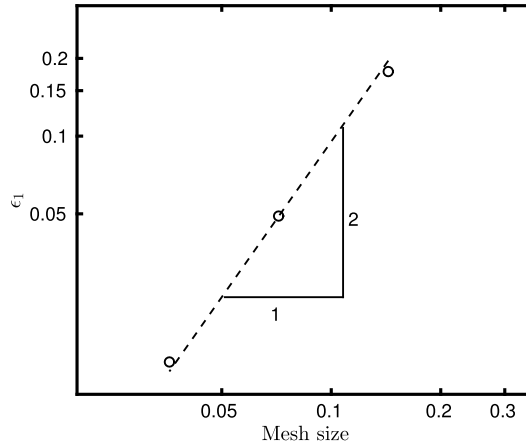


Fig. 9. Mesh convergence of FSI-III case for non-matching meshes using hybrid CR-NIFC formulation. The dotted line indicates a theoretical second-order accuracy.

$$u^f(0, y) = 1.5\bar{U} \frac{y(H-y)}{(\frac{H}{2})^2} = 1.5\bar{U} \frac{4.0}{0.1681} y(0.41-y), \quad (44)$$

where u^f is the X-component of the fluid velocity $\bar{\mathbf{u}}^f = (u^f, v^f, w^f)$, \bar{U} denotes the mean inlet velocity and $H = 4.1D$ is the height of the computational domain between Γ_{top} and Γ_{bottom} .

We decompose both the fluid and solid domains through finite element meshes. There is a boundary layer mesh surrounding the cylinder-bar and a triangular mesh outside the boundary layer region. Mesh convergence study is conducted to ensure that a sufficient mesh resolution is employed for both the fluid and solid subdomains. To eliminate the effect of the non-matching discretization, matching meshes are used to verify the fluid–structure coupling. Fig. 8b shows a typical mesh used for the verification study. Three sets of matching meshes with increasing element numbers are selected for this numerical study. Their characteristic responses are shown in Table 5. It is concluded that M3 has achieved sufficient convergence, therefore it is used as the reference case in our study.

To further demonstrate the accuracy of our implementation, the error for the response frequency is plotted in Fig. 9 as a function of mesh size. It is defined as follows:

$$\epsilon_1 = \frac{|f_y - f_{y,M3}|}{f_{y,M3}}, \quad (45)$$

where f_y is the frequency of the cross-flow displacement collected for five consecutive periods, and $f_{y,M3}$ corresponds to the reference value obtained with the mesh M3. It is found that our result is slightly deviated from the theoretical second-order accuracy, which can be attributed to other spatial and temporal discretization errors of the nonlinear coupled fluid–structure system. The computed values of maximum tip displacements ($A_{x,max}$ and $A_{y,max}$) and the transverse frequency f_y are overall in good agreement with the benchmark solutions. To further verify the accuracy of our FSI solver for the M3 mesh, the tip displacement history of the bar is plotted against the benchmark result in Fig. 10. In general, there is good agreement for both the displacement components between the present and the benchmark solutions.

Next, we proceed to quantify the accuracy of the FSI simulation when non-matching meshes with different mesh ratios are employed. A typical mesh used for this study is shown in Fig. 11. A series of numerical experiments are carried out by considering the mesh ratio ranging from 0.25 to 4.0 to capture both the situations where the load is transferred from the coarse mesh to the fine mesh and vice-versa. The characteristic response data of tip displacements and the frequency for each mesh ratio h_s/h_f are summarized in Table 6.

It is evident that the characteristic response values are close to each other for the range of mesh ratios h_s/h_f . Comparison of instantaneous Z-vorticity contours among the representative mesh ratios ($h_s/h_f = 0.5, 1.0, 2.0$) is illustrated in Fig. 12. These flow contours are plotted at the instant where the tip of the bar reaches its maximum displacement. We

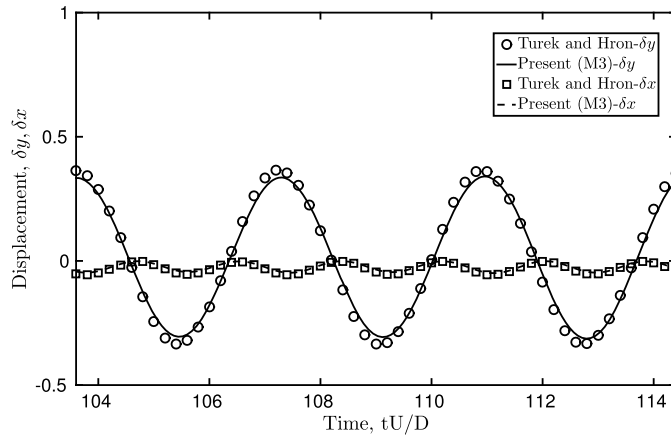


Fig. 10. Comparisons of tip displacements between the present study using M3 mesh and the reference data.

Table 6
Sensitivity and assessment of FSI results for varying mesh ratios h_s/h_f .

h_s/h_f	Fluid elements	Solid elements	$A_{x,max}$	$A_{y,max}$	f_y
4.0	25882	136	2.45	32.73	5.467
2.0	25882	544	2.47	32.97	5.455
1.0	25882	1280	2.45	32.89	5.468
0.5	25882	5120	2.46	32.95	5.455
0.25	25882	20480	2.44	32.98	5.442

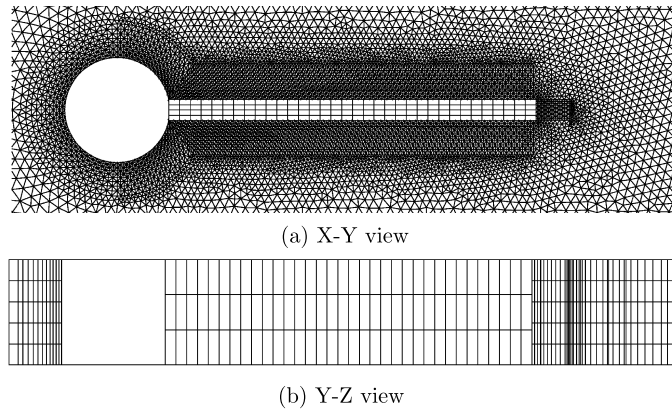


Fig. 11. A representative non-matching mesh configuration for the cylinder-bar system.

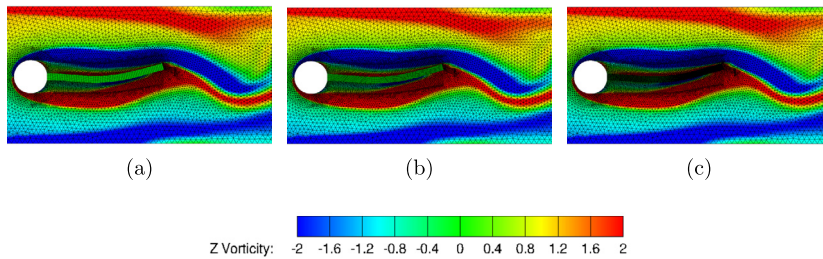


Fig. 12. Instantaneous Z-vorticity contours and meshes for representative mesh ratio: (a) fine to coarse mesh, $h_s/h_f = 2.0$, (b) matching mesh, $h_s/h_f = 1.0$, (c) coarse to fine mesh, $h_s/h_f = 0.5$. (For interpretation of the colors in the figure(s), the reader is referred to the web version of this article.)

can see that the flow patterns are very similar for different mesh ratios, thus indicating the qualitative accuracy of the 3D common-refinement method. In what follows, we demonstrate the accuracy and stability of the proposed CR-NIFC formulation to a large-scale 3D fluid–structure interaction of long flexible offshore riser with turbulent wake flow and strong added-mass effects.

7. Application to offshore riser VIV

The prediction of VIV of an offshore riser is crucial to prevent operational failure in a complex ocean environment. In this section, we demonstrate that our fluid–solid coupled FEM solver with the 3D common-refinement method is capable of predicting the dynamics of a riser with reasonable accuracy. To achieve this, we simulate a riser under uniform flow conditions which was carried out as a part of an experimental campaign in [59]. A schematic diagram of the riser setup is shown in Fig. 13. Consider the diameter of the circular riser to be D . The inlet (Γ_{in}) and outlet (Γ_{out}) boundaries are at a distance of $10D$ and $30D$ from the center of the cylindrical riser. The side boundaries are equidistant from the center of the riser at $10D$ corresponding to 5% blockage ratio. The riser spans in Z -direction, with its spanwise length, L equal to $481.5D$. Let the components of the fluid velocity be given as $\mathbf{u}^f = (u^f, v^f, w^f)$. A freestream velocity $u^f = U$ along the X -axis is imposed at the inlet boundary Γ_{in} . The top and bottom boundaries, Γ_{top} and Γ_{bottom} have slip boundary condition, where $\frac{\partial u^f}{\partial y} = 0$ and $v^f = 0$. The outlet Γ_{out} has a traction-free boundary condition, where $\sigma_{xx} = \sigma_{yx} = \sigma_{zx} = 0$. A pinned–pinned boundary condition is implemented on both the ends of the riser, with a tension, T applied at the top of the riser, while the no-slip condition is applied on the riser surface.

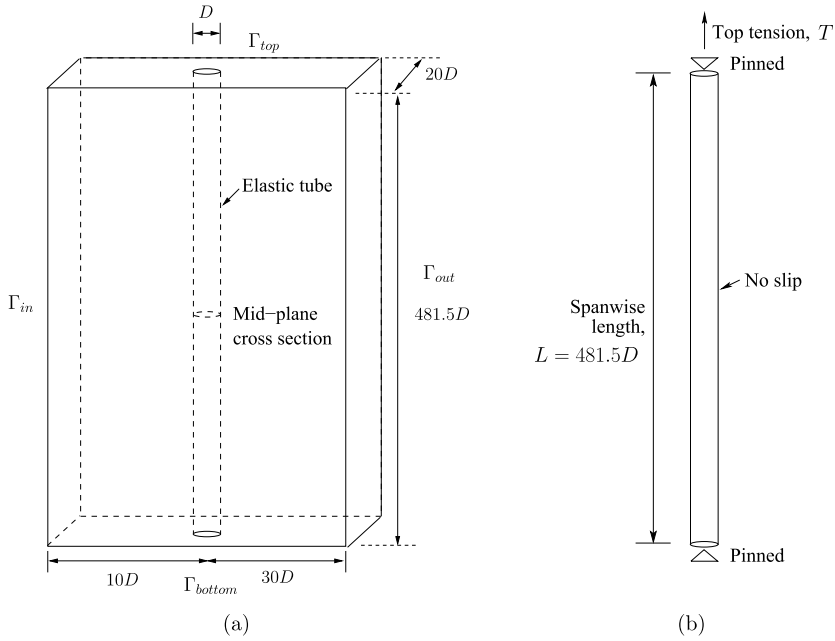


Fig. 13. Flow past a flexible offshore riser: (a) schematic of computational setup, (b) boundary conditions applied on the pinned–pinned tensioned riser.

A representative discretization of the fluid and structural mesh is shown in Fig. 14. The number of divisions on the circumference of the cross-section of the riser on the fluid and solid meshes is 96 and 120 respectively. A boundary layer is maintained along the riser such that $y^+ < 1$ in the wall-normal direction. The fluid domain is discretized into 9×10^5 nodes with 1.2×10^6 unstructured hexahedral elements, and the riser is discretized into 8.7×10^4 nodes with 9.7×10^4 hexahedral elements. Both the fluid and the riser are discretized into 100 layers in the spanwise direction. The non-dimensional time step is selected as $\Delta t U / D = 0.1$. The dimensionless parameters used in the simulation are:

$$Re = \frac{\rho^f U D}{\mu^f} = 4000, \quad \frac{EI}{\rho^f U^2 D^4} = 2.1158 \times 10^7, \quad (46)$$

$$\frac{T}{\rho^f U^2 D^2} = 5.10625 \times 10^4, \quad m^* = \frac{m^s}{\frac{\pi}{4} D^2 L \rho^f} = 2.23, \quad (47)$$

where I is the second moment of area of the riser's cross section and m^s is the mass of the riser. Key coupled dynamical results of the simulation are discussed in the following sections.

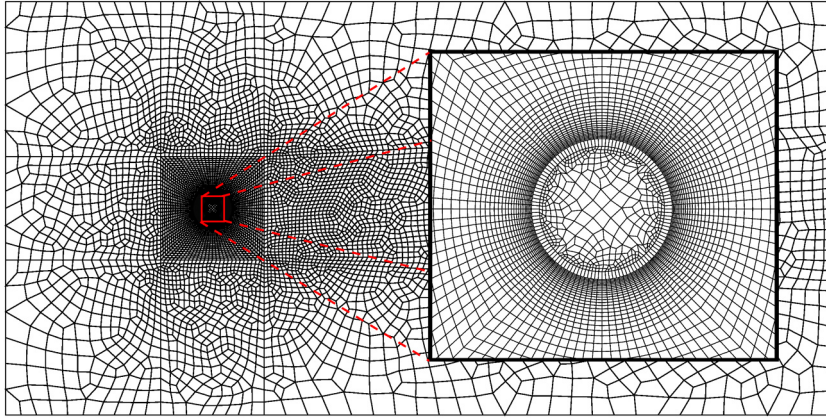


Fig. 14. A long riser under uniform flow: two-dimensional layer of the unstructured non-matching computational mesh. The inset shows the magnified view of the non-matching fluid–structure interface. The mesh is extruded in the third-dimension while maintaining a non-matching spanwise mesh.

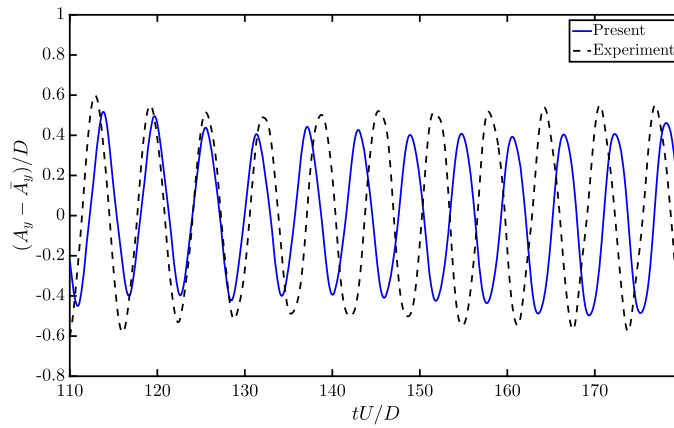


Fig. 15. Riser response under uniform current flow: time history of the cross-flow displacement at $z/L = 0.55$.

7.1. Response characteristics

The response along the riser is analyzed and compared to that of the experiment in this section. Fig. 15 shows a comparison of the time history of the cross-flow displacement at the position $z/L = 0.55$ between the present simulation and the experiment. We observe a multi-frequency response which is reflected by the spectral analysis carried out for the identical response in Fig. 16a. Furthermore, we observe that the in-line response frequency ($fD/U = 0.3516$) is twice that of the cross-flow frequency ($fD/U = 0.1758$). We also compare the root mean square values of the riser response with that of the experiment. Consider A_x and A_y as the displacement amplitudes at a point along the riser in the in-line and cross-flow directions, respectively. Let the temporal mean of the in-line and cross-flow amplitudes at the location be denoted by \bar{A}_x and \bar{A}_y , respectively. The root mean square values are calculated as

$$A_{x,\text{rms}} = \sqrt{\frac{1}{N} \sum_{i=1}^N (A_{x,i} - \bar{A}_x)^2}, \quad A_{y,\text{rms}} = \sqrt{\frac{1}{N} \sum_{i=1}^N (A_{y,i} - \bar{A}_y)^2}, \quad (48)$$

where N represents the number of samples collected in the time domain. The rms values are plotted in Fig. 16b. Although it shows a good agreement for the cross-flow amplitude, some over-prediction of the in-line amplitude is observed. This difference may be due to the sensitivity in the measurement of the in-line amplitude and the boundary layer characteristics along the flexible riser.

The response envelope of the riser is depicted in Fig. 17. We infer that the riser vibrates in a dominant second mode in the in-line direction and the first mode in the cross-flow direction which corroborates our observation of dual resonance from the spectral analysis. The riser response along the span of the riser with time is also shown in Fig. 18. We observe a standing wave-like pattern in the response.

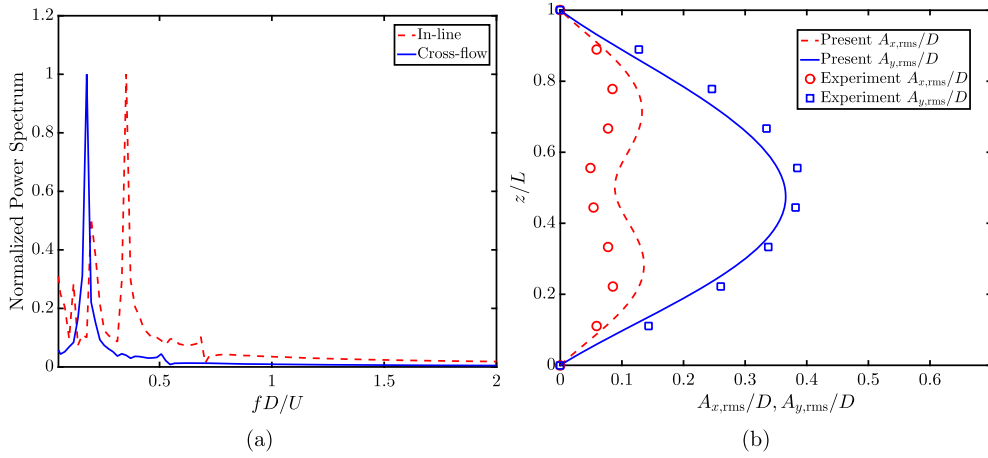


Fig. 16. Riser response under uniform current flow at $Re = 4000$: (a) power spectrum of the in-line and the cross-flow amplitudes along the riser, (b) comparison of the root mean square values of the in-line and cross-flow displacements along the riser with that of the experiment.

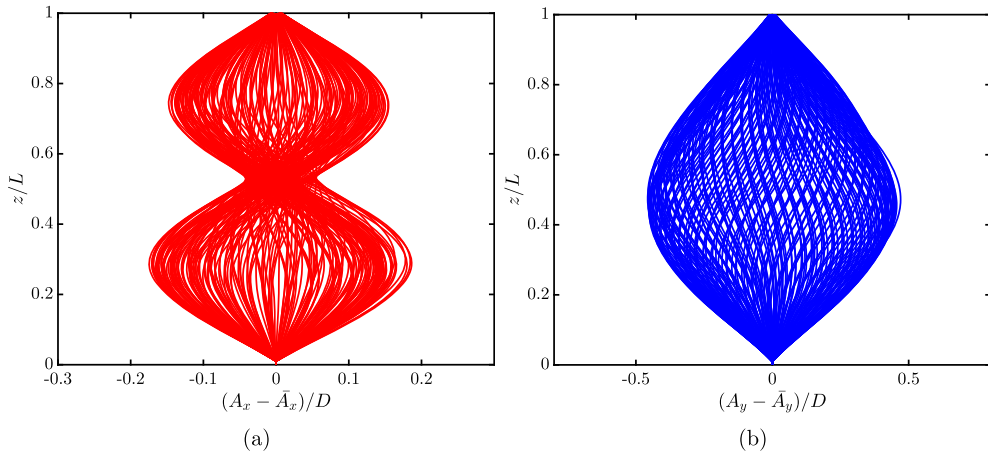


Fig. 17. Riser response envelope under uniform current flow: (a) in-line and (b) cross-flow directions. The riser is vibrating in the fundamental mode for the cross-flow, and the second mode for the in-line directions.

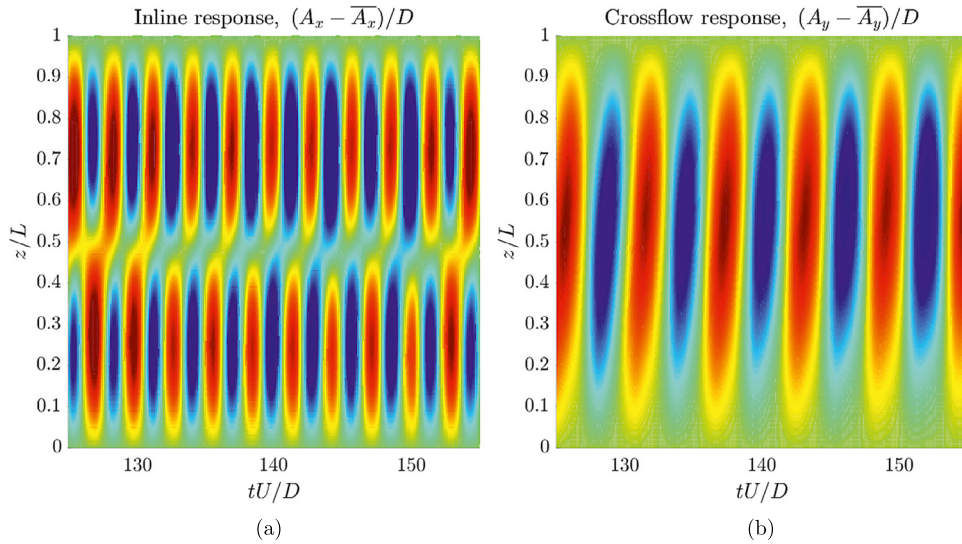


Fig. 18. Standing wave riser response under uniform current flow: (a) in-line; (b) cross-flow.

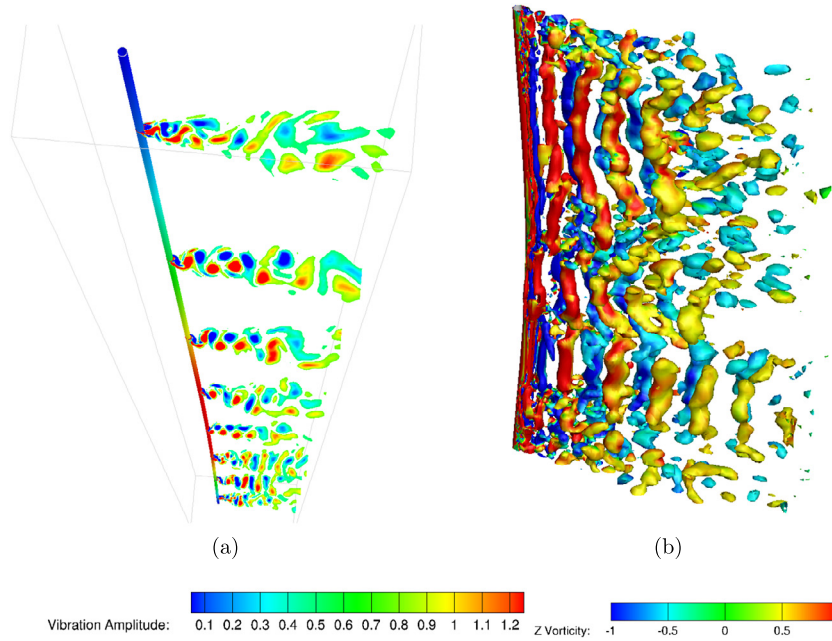


Fig. 19. (a) Vibration amplitude (surface of riser) and Z-vorticity contours (cross section) at different positions along the riser; (b) Instantaneous isosurfaces of $Q \left(-\frac{1}{2} \frac{\partial u_i}{\partial x_j} \frac{\partial u_j}{\partial x_i} \right)$ at $Q = 0.1$, colored by Z-vorticity.

7.2. Vortex patterns

In this section, we provide some insight into the flow visualization and the vortex patterns observed along the riser. The Z-vorticity contours at locations $z/L \in [0.11, 0.88]$ along with the vibration amplitude along the riser is displayed in Fig. 19a. We observe the 2S mode of vortex shedding in most of the locations along the riser while more complex shedding patterns are observed near the location with large amplitude. A 2P vortex mode is also observed in some locations. A further analysis is required to study the vortex dynamics in detail. The isosurfaces of Q-criterion colored by the Z-vorticity are shown in Fig. 19b. We observe more intense vortical structures near the location of large response amplitude. A more detailed analysis of the response amplitude and its relation to the trajectories along the riser can be found in [60]. This demonstration concludes that the present solver with the common-refinement method can capture the physics as well as the response of the flexible riser reasonably well for non-matching unstructured meshes.

8. Conclusions

In this paper, a combined 3D common-refinement method with nonlinear iterative force correction is presented for the non-matching interface between the partitioned finite-element subdomains of incompressible flow and nonlinear hyper-elastic structure. Owing to the weighted residual formulation in three dimensions, the common-refinement method has good accuracy for fluid–structure interactions. The current implementation can be used for a wide range of FSI applications while retaining the modularity of both physical systems and the flexibility of non-matching meshes. We have shown that the 3D common-refinement method provides an accurate coupling by minimizing the error in the transfer of data in the ℓ_2 norm across the overlay surface between the fluid and the structure meshes. Through a systematic error analysis, the common-refinement method was shown to be consistent in terms of overall accuracy for three-dimensional data transfer. The second-order spatial accuracy of the common-refinement method has been confirmed for different mesh ratios. The common-refinement method was then combined with the nonlinear iterative force correction procedure to solve FSI problems with strong added-mass effects associated with low structure-to-fluid density ratio. The overall implementation was verified against the reference benchmark data for the cylinder-bar problem. Accuracy and stability of the hybrid common-refinement method and NIFC has been demonstrated for the cylinder-bar system for a range of mesh ratios along the fluid–solid interface. We demonstrated the applicability of the hybrid CR-NIFC formulation to large 3D simulations of an offshore riser problem with non-matching meshes. The combined common-refinement and NIFC method provided a stable solution for the 3D flexible riser in turbulent flow with a strong inertial coupling of the surrounding wake flow. The cross-flow amplitude of flexible riser agreed reasonably well with the measurement data. To improve the efficiency of coupled FSI framework for high-gradient physics, it will be worth developing adaptive 3D non-matching meshes across the fluid–structure interface.

Acknowledgements

The authors would like to acknowledge the Singapore Maritime Institute Grant (SMI-2014-OF-03) for the financial support. We also thank the National Research Foundation, Keppel Corporation and National University of Singapore for a partial support of this work done in the Keppel–NUS Corporate Laboratory. The computational work for this article was partially performed on resources of the National Supercomputing Centre, Singapore (<https://www.nsc.sg>). The conclusions put forward reflect the views of the authors alone, and not necessarily those of the institutions within the Corporate Laboratory. The first author appreciates the help from Prof. Allan Bower on the hyperelastic theory and its computer implementation.

Appendix A. The relevance of consistent load transfer into energy stability

To support the energy stability in fluid–structure interaction, we provide the relevance of the consistency and conservation of load transfer across non-matching meshes via the common-refinement integration. We begin with the interface conditions that are weakly satisfied at the fluid–structure interface (Eq. (8) and (9)) at the intermediate temporal locations $n + \alpha^f$ and $n + \alpha^s$ as follows:

$$\bar{\mathbf{u}}^{f,n+\alpha^f} = \mathbf{u}^{s,n+\alpha^s}, \quad (\text{A.1})$$

$$\int_{\varphi^s(\gamma,t)} \boldsymbol{\sigma}^{f,n+\alpha^f} \cdot \mathbf{n} d\Gamma + \int_{\gamma'} \mathbf{t}^{s,n+\alpha^s} d\Gamma = \mathbf{0}. \quad (\text{A.2})$$

While the velocity continuity is satisfied pointwise, the traction equilibrium condition is satisfied over the sub-element constructed at the common-refinement boundary (Eq. (35)). For simplicity, we assume that $\alpha^f = \alpha^s = \alpha$. Equation (A.1) then can be simplified as

$$\mathbf{u}^{f,n+1} - \mathbf{u}^{s,n+1} = -\frac{1-\alpha}{\alpha}(\mathbf{u}^{f,n} - \mathbf{u}^{s,n}). \quad (\text{A.3})$$

Following the discussion in [34], the load transfer integral is assumed to be evaluated with sufficient accuracy. This allows us to neglect the numerical integration error in the present analysis. Thus, a locally accurate traction equilibrium across the common-refinement boundary can be expressed as

$$\boldsymbol{\sigma}^{f,n+\alpha} \cdot \mathbf{n} + \mathbf{t}^{s,n+\alpha} = \mathbf{0}, \quad (\text{A.4})$$

$$\Rightarrow \boldsymbol{\sigma}^{f,n+1} \cdot \mathbf{n} + \mathbf{t}^{s,n+1} = -\frac{1-\alpha}{\alpha}(\boldsymbol{\sigma}^{f,n} \cdot \mathbf{n} + \mathbf{t}^{s,n}). \quad (\text{A.5})$$

Next, we define the measure for residual work at $(n+1)$ similar to the work carried out in [34] as

$$W^{n+1} = \left| \int_{\Gamma^{fs}} (\mathbf{u}^{f,n+1} - \mathbf{u}^{s,n+1})(\boldsymbol{\sigma}^{f,n+1} \cdot \mathbf{n} + \mathbf{t}^{s,n+1}) d\Gamma \right|, \quad (\text{A.6})$$

which represents the product of residuals in the load transfer and velocity continuity. Note that the integration is taken over the reference surface, Γ^{fs} , which is a common-refinement interface of both fluid and solid surfaces. From the Cauchy–Schwarz inequality, we get

$$W^{n+1} \leq \left[\int_{\Gamma^{fs}} |\mathbf{u}^{f,n+1} - \mathbf{u}^{s,n+1}| d\Gamma \right] \left[\int_{\Gamma^{fs}} |\boldsymbol{\sigma}^{f,n+1} \cdot \mathbf{n} + \mathbf{t}^{s,n+1}| d\Gamma \right], \quad (\text{A.7})$$

where the right hand side is the upper bound for the residual work at $(n+1)$ th iteration. Let us denote it as I^{n+1} . Therefore, we have

$$I^{n+1} = \left[\int_{\Gamma^{fs}} |\mathbf{u}^{f,n+1} - \mathbf{u}^{s,n+1}| d\Gamma \right] \left[\int_{\Gamma^{fs}} |\boldsymbol{\sigma}^{f,n+1} \cdot \mathbf{n} + \mathbf{t}^{s,n+1}| d\Gamma \right]. \quad (\text{A.8})$$

Substituting Eqs. (A.3) and (A.5) in Eq. (A.8),

$$I^{n+1} = \left(\frac{1-\alpha}{\alpha} \right)^2 \left[\int_{\Gamma^{fs}} |\mathbf{u}^{f,n} - \mathbf{u}^{s,n}| d\Gamma \right] \left[\int_{\Gamma^{fs}} |\boldsymbol{\sigma}^{f,n} \cdot \mathbf{n} + \mathbf{t}^{s,n}| d\Gamma \right], \quad (\text{A.9})$$

$$I^{n+1} = \left(\frac{1-\alpha}{\alpha} \right)^2 I^n. \quad (\text{A.10})$$

With the aid of the properties of the generalized- α parameters (Eq. (13)), it can be observed that $(1 - \alpha)/\alpha \leq 1$, which implies

$$I^{n+1} \leq I^n. \quad (\text{A.11})$$

Hence, the consistent and conservative integration of the load transfer along the common-refinement interface achieves the energy stability across non-matching meshes in fluid–structure interaction problems.

References

- [1] S.-C. Lee, M.N. Vouvakis, J.-F. Lee, A non-overlapping domain decomposition method with non-matching grids for modeling large finite antenna arrays, *J. Comput. Phys.* 203 (1) (2005) 1–21.
- [2] Z. Peng, J.-F. Lee, Non-conformal domain decomposition method with second-order transmission conditions for time-harmonic electromagnetics, *J. Comput. Phys.* 229 (16) (2010) 5615–5629.
- [3] S. Hueber, B.I. Wohlmuth, Thermo-mechanical contact problems on non-matching meshes, *Comput. Methods Appl. Mech. Eng.* 198 (15) (2009) 1338–1350.
- [4] N. El-Abbasi, K.-J. Bathe, Stability and patch test performance of contact discretizations and a new solution algorithm, *Comput. Struct.* 79 (2001) 1473–1486.
- [5] B. Flemisch, M.A. Puso, B.I. Wohlmuth, A new dual mortar method for curved interfaces: 2D elasticity, *Int. J. Numer. Methods Eng.* 63 (2005) 813–832.
- [6] I. Lee, J.H. Roh, I.K. Oh, Aerothermoelastic phenomena of aerospace and composite structures, *J. Therm. Stresses* 26 (2003) 526–546.
- [7] R.K. Jaiman, X. Jiao, P.H. Geubelle, E. Loth, Conservative load transfer along curved fluid–solid interface with nonmatching meshes, *J. Comput. Phys.* 218 (2006) 372–397.
- [8] R.K. Jaiman, F. Shakib, O.H. Oakley, Y. Constantinides, Fully coupled fluid–structure interaction for offshore applications, in: *ASME Offshore Mechanics and Arctic Engineering OMAE09-79804 CP*, 2009.
- [9] Y.Z. Law, R.K. Jaiman, Wake stabilization mechanism of low-drag suppression devices for vortex-induced vibration, *J. Fluids Struct.* 70 (2017) 428–449.
- [10] R.D. Blevins, *Flow-Induced Vibration*, Van Nostrand Reinhold Co., Inc., New York, 1990.
- [11] F.J. Blom, A monolithic fluid–structure interaction algorithm applied to the piston problem, *Comput. Methods Appl. Mech. Eng.* 167 (1998) 369–391.
- [12] B. Hübner, E. Walhorn, D. Dinkler, A monolithic approach to fluid–structure interaction using space–time finite elements, *Comput. Methods Appl. Mech. Eng.* 193 (23) (2004) 2087–2104.
- [13] J. Hron, S. Turek, *A Monolithic FEM/Multigrid Solver for an ALE Formulation of Fluid–Structure Interaction with Applications in Biomechanics*, Springer, 2006.
- [14] J. Liu, R.K. Jaiman, P.S. Gurugubelli, A stable second-order scheme for fluid–structure interaction with strong added-mass effects, *J. Comput. Phys.* 270 (2014) 687–710.
- [15] P.S. Gurugubelli, R.K. Jaiman, Self-induced flapping dynamics of a flexible inverted foil in a uniform flow, *J. Fluid Mech.* 781 (2015) 657–694.
- [16] C.A. Felippa, K.C. Park, C. Farhat, Partitioned analysis of coupled mechanical systems, *Comput. Methods Appl. Mech. Eng.* 190 (2001) 3247–3270.
- [17] J.R. Cebal, R. Lohner, Conservative load projection and tracking for fluid–structure problems, *AIAA J.* 35 (4) (1997) 687–692.
- [18] C. Farhat, K.G. van der Zee, P. Geuzaine, Provably second-order time-accurate loosely-coupled solution algorithms for transient nonlinear computational aeroelasticity, *Comput. Methods Appl. Mech. Eng.* 195 (2006) 1973–2001.
- [19] S. Piperno, C. Farhat, Partitioned procedures for the transient solution of coupled aeroelastic problems Part 1: Model problem, theory, and two-dimensional application, *Comput. Methods Appl. Mech. Eng.* 124 (1995) 79–112.
- [20] A. Yenduri, R. Ghoshal, R.K. Jaiman, A new partitioned staggered scheme for flexible multibody interactions with strong inertial effects, *Comput. Methods Appl. Mech. Eng.* 315 (2017) 316–347.
- [21] R.K. Jaiman, S. Sen, P.S. Gurugubelli, A fully implicit combined field scheme for freely vibrating square cylinders with sharp and rounded corners, *Comput. Fluids* 112 (2015) 1–18.
- [22] R.K. Jaiman, P.H. Geubelle, E. Loth, X. Jiao, Combined interface condition method for unsteady fluid–structure interaction, *Comput. Methods Appl. Mech. Eng.* 200 (2011) 27–39.
- [23] R.K. Jaiman, N.R. Pillalamarri, M.Z. Guan, A stable second-order partitioned iterative scheme for freely vibrating low-mass bluff bodies in a uniform flow, *Comput. Methods Appl. Mech. Eng.* 301 (2016) 187–215.
- [24] M.A. Fernández, J.-F. Gerbeau, C. Grandmont, A projection algorithm for fluid–structure interaction problems with strong added-mass effect, *C. R. Math.* 342 (4) (2006) 279–284.
- [25] M.A. Fernández, J.-F. Gerbeau, C. Grandmont, A projection semi-implicit scheme for the coupling of an elastic structure with an incompressible fluid, *Int. J. Numer. Methods Eng.* 69 (4) (2007) 794–821.
- [26] H. Baek, G.E. Karniadakis, A convergence study of a new partitioned fluid–structure interaction algorithm based on fictitious mass and damping, *J. Comput. Phys.* 231 (2) (2012) 629–652.
- [27] S. Badia, A. Quaini, A. Quarteroni, Splitting methods based on algebraic factorization for fluid–structure interaction, *SIAM J. Sci. Comput.* 30 (4) (2008) 1778–1805.
- [28] S. Badia, A. Quaini, A. Quarteroni, Modular vs. non-modular preconditioners for fluid–structure systems with large added-mass effect, *Comput. Methods Appl. Mech. Eng.* 197 (49) (2008) 4216–4232.
- [29] G. Guidoboni, R. Glowinski, N. Cavallini, S. Canic, Stable loosely-coupled-type algorithm for fluid–structure interaction in blood flow, *J. Comput. Phys.* 228 (18) (2009) 6916–6937.
- [30] H.G. Matthies, R. Niekamp, J. Steindorf, Algorithms for strong coupling procedures, *Comput. Methods Appl. Mech. Eng.* 195 (2006) 2028–2049.
- [31] H. Ahn, Y. Kallinderis, Strongly coupled flow/structure interactions with a geometrically conservative ALE scheme on general hybrid meshes, *J. Comput. Phys.* 219 (2006) 671–696.
- [32] C. Farhat, M. Lesoinne, P. Le Tallec, Load and motion transfer algorithms for fluid/structure interaction problems with non-matching discrete interfaces: Momentum and energy conservation, optimal discretization and application to aeroelasticity, *Comput. Methods Appl. Mech. Eng.* 157 (1–2) (1998) 95–114.
- [33] A. De Boer, A. Van Zuijlen, H. Bijl, Review of coupling methods for non-matching meshes, *Comput. Methods Appl. Mech. Eng.* 196 (8) (2007) 1515–1525.
- [34] R.K. Jaiman, X. Jiao, P.H. Geubelle, E. Loth, Conservative load transfer along curved fluid–solid interface with non-matching meshes, *J. Comput. Phys.* 218 (1) (2006) 372–397.
- [35] R.K. Jaiman, X. Jiao, P.H. Geubelle, E. Loth, Assessment of conservative load transfer for fluid–solid interface with non-matching meshes, *Int. J. Numer. Methods Eng.* 64 (15) (2005) 2014–2038.
- [36] X. Jiao, M.T. Heath, Common-refinement-based data transfer between non-matching meshes in multiphysics simulations, *Int. J. Numer. Methods Eng.* 61 (14) (2004) 2402–2427.

- [37] X. Jiao, M.T. Heath, Overlaying surface meshes, Part I: Algorithms, *Int. J. Comput. Geom. Appl.* 14 (06) (2004) 379–402.
- [38] S.R. Slattery, Mesh-free data transfer algorithms for partitioned multiphysics problems: Conservation, accuracy, and parallelism, *J. Comput. Phys.* 307 (2016) 164–188.
- [39] X. Jiao, M.T. Heath, Overlaying surface meshes, Part II: Topology preservation and feature matching, *Int. J. Comput. Geom. Appl.* 14 (06) (2004) 403–419.
- [40] E.H. van Brummelen, Added mass effects of compressible and incompressible flows in fluid–structure interaction, *J. Appl. Mech.* 76 (2009) 02106.
- [41] R.K. Jaiman, M.K. Parmar, P.S. Gurugubelli, Added mass and aeroelastic stability of a flexible plate interacting with mean flow in a confined channel, *J. Appl. Mech.* 81 (2014) 041006.
- [42] C. Forster, W.A. Wall, E. Ramm, Artificial added mass instabilities in sequential staggered coupling of nonlinear structures and incompressible viscous flows, *Comput. Methods Appl. Mech. Eng.* 196 (2007) 1278–1293.
- [43] P. Causin, J.F. Gerbeau, F. Nobile, Added-mass effect in the design of partitioned algorithms for fluid–structure problems, *Comput. Methods Appl. Mech. Eng.* 194 (2005) 4506–4527.
- [44] R.K. Jaiman, M.Z. Guan, T.P. Miyanawala, Partitioned iterative and dynamic subgrid-scale methods for freely vibrating square-section structures at subcritical Reynolds number, *Comput. Fluids* 133 (2016) 68–89.
- [45] T.J.R. Hughes, W. Liu, T. Zimmerman, Lagrangian–Eulerian finite element formulation for incompressible viscous flows, *Comput. Methods Appl. Mech. Eng.* 29 (1981) 329–349.
- [46] J. Donea, S. Giuliani, J.P. Halleux, Arbitrary Lagrangian–Eulerian finite element method for transient dynamic fluid–structure interactions, *Comput. Methods Appl. Mech. Eng.* 33 (1982) 689–723.
- [47] E. Kuhl, H. Askes, P. Steinmann, An ALE formulation based on spatial and material settings of continuum mechanics. Part 1: Generic hyperelastic formulation, *Comput. Methods Appl. Mech. Eng.* 193 (39) (2004) 4207–4222.
- [48] A.F. Bower, *Applied Mechanics of Solids*, CRC Press, 2009.
- [49] K.E. Jansen, C.H. Whitting, G.M. Hulbert, A generalized- α method for integrating the filtered Navier–Stokes equations with a stabilized finite element method, *Comput. Methods Appl. Mech. Eng.* 190 (2000) 305–319.
- [50] Y. Bazilevs, K. Takizawa, T.E. Tezduar, *Computational Fluid–Structure Interaction: Methods and Applications*, Wiley, 2013.
- [51] S.S. Antman, *Nonlinear Problems of Elasticity*, Springer-Verlag, New York, 2005.
- [52] C. Breziniski, M.R. Zaglia, Generalizations of Aitken's process for accelerating the convergence of sequence, *J. Comput. Appl. Math.* 26 (2007) 171–189.
- [53] D. Buoso, A. Karapiperi, S. Pozza, Generalizations of Aitken's process for a certain class of sequences, *Appl. Numer. Math.* 90 (2015) 38–54.
- [54] Y. Saad, M.H. Schultz, GMRES: A generalized minimal residual algorithm for solving nonsymmetric linear systems, *SIAM J. Sci. Stat. Comput.* 7 (3) (1986) 856–869.
- [55] K. Woodsend, J. Gondzio, Hybrid MPI/OpenMP parallel linear support vector machine training, *J. Mach. Learn. Res.* 10 (Aug) (2009) 1937–1953.
- [56] G. Karypis, V. Kumar, A software package for partitioning unstructured graphs, partitioning meshes, and computing fill-reducing orderings of sparse matrices, University of Minnesota, Department of Computer Science and Engineering, Army HPC Research Center, Minneapolis, MN.
- [57] L. Smith, M. Bull, Development of mixed mode MPI/OpenMP applications, *Sci. Program.* 9 (2–3) (2001) 83–98.
- [58] S. Turek, J. Hron, Proposal for numerical benchmarking of fluid–structure interaction between an elastic object and laminar incompressible flow, in: *Fluid–Structure Interaction*, Springer, 2006, pp. 371–385.
- [59] Vortex induced vibration data repository, <http://web.mit.edu.sg/towtank/www/vivdr/downloadpage.html>, datasets from ExxonMobil (Test case 1103).
- [60] V. Joshi, R.K. Jaiman, A variationally bounded scheme for delayed detached eddy simulation: Application to vortex-induced vibration of offshore riser, *Comput. Fluids* 157 (2017) 84–111.